Title
Unleashing Type-2 Dendritic Cells to Drive Protective Antitumor CD4+ T Cell Immunity

Journal
Cell, 177(3)

ISSN
0092-8674

Authors
Binnewies, Mikhail
Mujal, Adriana M
Pollack, Joshua L
et al.

Publication Date
2019-04-01

DOI
10.1016/j.cell.2019.02.005

Peer reviewed

Published in final edited form as:

Cell. 2019 April 18; 177(3): 556–571.e16. doi:10.1016/j.cell.2019.02.005.

Unleashing Type-2 Dendritic Cells to Drive Protective Antitumor CD4+ T cell Immunity

Mikhail Binnewies[1,8], **Adriana M. Mujal**[1,7,8], **Joshua L. Pollack**[5], **Alexis J. Combes**[1,2], **Emily A. Hardison**[1], **Kevin C. Barry**[1,2], **Megan K. Ruhland**[1], **Kelly Kersten**[1], **Jessica Tsui**[1,2], **Marwan A. Abushawish**[6], **Marko Spasic**[3], **Jonathan P. Giurintano**[4], **Vincent Chan**[1,2], **Adil I. Daud**[3], **Patrick Ha**[4], **Chun J. Ye**[5], **Edward W. Roberts**[1], **Matthew F. Krummel**[1,2,‡]

[1]Department of Pathology, University of California San Francisco, San Francisco, CA 94143, USA

[2]UCSF Immunoprofiler Initiative, University of California San Francisco, San Francisco, CA 94143, USA

[3]Melanoma Clinical Research Unit, University of California San Francisco, San Francisco, CA 94143, USA

[4]Department of Otolaryngology, University of California San Francisco, San Francisco, CA 94143, USA

[5]Institute of Human Genetics, University of California San Francisco, San Francisco, CA 94143, USA

[6]Pionyr Immunotherapeutics, San Francisco, CA 94107, USA

[7]Present address: Immunology Program, Memorial Sloan Kettering Cancer Center, New York, NY, 10065, USA

[8]These authors contributed equally to this work

Summary

Differentiation of proinflammatory CD4$^+$ conventional T cells (T_{conv}) are critical for productive antitumor responses yet their elicitation remains poorly understood. We exhaustively characterized myeloid cells in tumor draining lymph nodes (tdLN) of mice and identified two subsets of conventional type-2 dendritic cells (cDC2) that traffic from tumor to tdLN and present tumor-derived antigens to CD4$^+$ T_{conv}, but then fail to support antitumor CD4$^+$ T_{conv} differentiation. Regulatory T cell (T_{reg}) depletion enhanced their capacity to elicit strong CD4$^+$ T_{conv} responses and ensuing antitumor protection. Analogous cDC2 populations were identified in patients, and as in mice their abundance relative to T_{reg} predicts protective ICOS$^+$ PD-1^{lo} CD4$^+$ T_{conv} phenotypes

‡To whom correspondence should be addressed. matthew.krummel@ucsf.edu.

Authorship Contribution

M.B., A.M.M. and M.F.K. designed experiments and M.B. and A.M.M. performed experiments unless specified. J.L.P. and C.J.Y. participated in the processing and analysis of single-cell RNA-sequencing samples. A.C. analyzed data related to human samples. E.A.H and J.T. performed tumor growth experiments. K.K., M.K.R., K.C.B., M.A.A. and E.W.R. participated in experimental preparation and analyzing flow cytometry. A.D., M.S., J.P.G., and P.H. facilitated acquisition of human tumor tissue. V.C. managed the acquisition and profiling of human tumors,. M.B., A.M.M and M.F.K, wrote, revised and edited the manuscript.

Data and Software Availability

Data Resources

The accession number for the expression matrix for the single-cell RNA-sequencing reported in this paper is GEO: XXXXXXXXX

and survival. Further, in melanoma patients with low T_{reg} abundance, intratumoral cDC2 density alone correlates with abundant $CD4^+$ T_{conv} and with responsiveness to anti-PD-1 therapy. Together, this highlights a pathway which restrains cDC2, and whose reversal enhances $CD4^+$ T_{conv} abundance and controls tumor growth.

Introduction

Adaptive T cell responses are critical for controlling tumor growth through production of inflammatory cytokines and direct cytolytic targeting. Recent therapeutic advances that block inhibitory T cell checkpoint molecules like CTLA-4 or PD-1/PD-L1 have demonstrated clinical success, but in only a subset of cancer patients (Hodi et al., 2008; Huang et al., 2017; Larkin et al., 2015; Topalian et al., 2014). Recent evidence suggests that tumors often promote the generation of dysfunctional and exhausted T cells with deficient effector capacity reminiscent of exhaustion observed following chronic viral infection (Schietinger et al., 2016). T cell exhaustion is enforced at the chromatin level such that many T cells in the tumor microenvironment (TME) are likely not able to be rescued by immune checkpoint blockades (ICB) (Pauken et al., 2016; Philip et al., 2017). Thus, in those patients with poor T cell infiltration or irreversibly exhausted T cells, additional steps, such as improving *de novo* priming of effector T cells, may be necessary to engage effective antitumor immunity (Philip et al., 2017; Tumeh et al., 2014).

While $CD8^+$ T cells are considered a primary immunotherapeutic target due to their classic role in tumor cell cytolysis, $CD4^+$ T_{conv} are emerging as an important contributor to antitumor responses. In immunogenic settings, effector $CD4^+$ T_{conv} augment immunity through licensing of dendritic cells (DC) (Behrens et al., 2004) and stimulating pro-inflammatory myeloid cell programs (Corthay et al., 2005). $CD4^+$ T_{conv} have also been documented to improve the quality of effector $CD8^+$ T cell responses to apoptotic cell antigens (a common source of tumor antigen) and contribute to T cell memory programming and maintenance (Laidlaw et al., 2016). Intriguingly, $CD4^+$ T_{conv} have been described as having direct antitumor cytolytic function(Curran et al., 2013; Quezada et al., 2010) and HLA-DR expression on human tumor cells (MHC-II in mouse) has been identified as a biomarker for anti-PD-1/PD-L1 responsiveness (Johnson et al., 2016). Notably, effective anti-CTLA-4 therapy results in a systemically circulating population of $ICOS^+$ $PD\text{-}1^{lo}$ $CD4^+$ T helper 1-like (T_h1-like) effector $CD4^+$ T_{conv} critical for an antitumor response (Fan et al., 2014). Conversely, presence of a $PD\text{-}1^{hi}$ $CD4^+$ T_{conv} phenotype, correlated with extensive tumor burden and likely T cell exhaustion, has been shown to be a negative prognostic indicator for checkpoint blockade (Zappasodi et al., 2018). As such, the processes that contributes to antitumor $CD4^+$ T_{conv} activation and differentiation merit further investigation.

Generation of newly activated antitumor T cell clones typically requires their activation in secondary lymphoid organs such as the tumor-draining lymph node (tdLN), followed by subsequent infiltration into the tumor mass (Chen and Mellman, 2013). Initiation of an adaptive T cell response is driven by one or more types of innate myeloid antigen-presenting cells (APC) such as conventional dendritic cells (cDC) that present tumor antigen, co-

stimulatory molecules, and cytokines to cognate antigen-specific T cells. Given the shortcomings in endogenously-generated antitumor T cell responses, there has long been therapeutic interest to improve cDC numbers and functionality as a means to boost T cell effector potential. Approaches such as cellular vaccines or administration of cDC growth factors, however, remain susceptible to endogenous immunosuppressive cells such as T_{reg} (Josefowicz et al., 2012) which can potently suppress cDC (Bauer et al., 2014), although given the complexity of cDC populations, it is currently unclear if specific populations of cDC are selectively impacted.

Diverse in nature, cDC can be broadly divided into cDC1 and cDC2 populations that arise through distinct pre-DC lineages (Schlitzer et al., 2015) and can be either resident to the LN, or migrate in from peripheral tissues bearing antigen (Merad et al., 2013). Importantly, cDC1 and cDC2 often take on specialized roles in $CD8^+$ T cell and $CD4^+$ T_{conv} priming processes through their differential use of antigen processing and presentation pathways (Gutierrez-Martinez et al., 2015), production of effector cytokines (Merad et al., 2013), and spatial localization within the LN (Gerner et al., 2017). cDC1 have been identified as critical for directing $CD8^+$ T cell immunity to various pathogens (Bedoui et al., 2009; Belz et al., 2005) and in mediating spontaneous antitumor $CD8^+$ T cell responses (Broz et al., 2014; Roberts et al., 2016; Ruffell et al., 2014; Salmon et al., 2016; Spranger et al., 2017). In contrast, cDC2 contain substantial heterogeneity and they preferentially initiate $CD4^+$ T_{conv} responses in a variety of immunological models (Gao et al., 2013; Krishnaswamy et al., 2017). While the division of labor between cDC1 and cDC2 in engaging $CD8^+$ T cells and $CD4^+$ T_{conv}, respectively, is an established phenomenon, this may depend on the tissue type and each may have multiple capabilities to tolerize or activate respective cells types, depending on the nature of the immune challenge. On the whole, the specific cDC roles in eliciting antitumor $CD4^+$ T_{conv} immunity remains unresolved.

We therefore applied single-cell RNA-sequencing (scRNA-seq) to myeloid populations from tdLNs in mouse and human to understand the true diversity and function of cell types present, how they differ with cancer, and how the variance might affect the nature of the $CD4^+$ T_{conv} that are available for tumor efficacy. Key in this was to understand how therapeutic intervention might alter the outcome of $CD4^+$ T_{conv} priming. Additionally, we sought to understand whether human cancer biology paralled the mouse and assembled cohorts of patient biopies to determine how $CD4^+$ T_{conv} phenotype and cDC composition were connected.

Results

Myeloid heterogeneity at single cell resolution

To comprehensively study the myeloid populations capable of priming anti-tumor $CD4^+$ T_{conv}, we queried myeloid heterogeneity in the tdLN by sorting non-lymphocyte ($CD90.2^-$ $B220^-$ $NK1.1^-$) myeloid cells ($CD11c^+$ or $CD11b^+$) from the tdLN of B16-F10 tumor-bearing mice. We performed scRNA-seq using the 10X Genomics Chromium platform paired with deep sequencing. Analysis of 4133 tdLN myeloid cells yielded 10 high quality and unique population clusters (Figure 1A, S1A).

To rigorously identify the myeloid populations and determine how they related to those previously described in other settings, we generated gene signatures of cell populations expected to be present in the LN from samples available from the Immunological Genome Project (ImmGen) database (Heng and Painter, 2008) and plotted expression of these signatures on the tdLN *t*-SNE plot. This allowed us to assign cellular identities to each cluster (Figure 1B and **Table 1**), apart from clusters 8 and 9, as they appeared to be lymphocyte contaminates and were excluded from further analysis (data not shown).

We then utilized gene overlays of individual canonical myeloid markers to further explore the cluster identities. *Ccr7* and *Itgax* demarcarcated migratory (clusters 0, 1, 2, 4 and 6) and resident (clusters 3, 5 and 7) DCs, consistent with our assignments and the known biology (Figure S1B). DC clusters (0–4, 6–7) were further confirmed using canonical genes *Zbtb46* and *Flt3,* whereas monocytes and T cell zone macrophages (TZ Macrophages), which are unable to prime $CD4^+$ T_{conv} (Baratin et al., 2017), both occupied cluster 5, but localized to opposite sides of the cluster (Figure S1C).

We performed differential expression (DE) analysis for each myeloid cluster versus all other clusters and generated heatmaps for the top 10 most differentially expressed genes (Figure 1C and **Table 2**). In addition to highlighting key genes that contributed to the unbiased segregation of these populations, a number of markers also validated previous reports of specialized cellular functions such as production of *Il12b* in $mCD103^+$ cDC1(Miller et al., 2012) or *Ccl17* in $CD11b^+$ cDC2 and mLC (Alferink et al., 2003). Moreover, there was a general pattern of shared transcriptional identity within resident and migratory populations, which was further elucidated by performing DE analysis between migratory (clusters 0, 1, 2, 4 and 6) and resident (clusters 3 and 7) DC populations (Figure S1D and **Table 3**). Expression was largely uniform within migratory and resident DC, with enrichment of genes previously associated with migratory populations such as *Socs2* or *Fscn1* (Miller et al., 2012).

Populations identified through unbiased clustering largely mirrored those identified using ImmGen-based criteria. However, of specific note, and in contrast to migratory cDC1, the canonical signature for migratory cDC2 applied to multiple clusters in our unbiased analysis. This indicated substantial and unresolved heterogeneity within this cDC class. DE analysis between migratory $CD11b^+$ cDC2 clusters 0 and 4 identified the gene *Cd9,* a surface molecule, to be expressed specifically on cluster 0 (Figure 1D and **Table 4**). We determined that surface expression of CD9 parsed the two $CD11b^+$ cDC2 populations and with further investigation we found that expression was concordant with a previously identified molecule that distinguished cDC2 subsets, CD301b (Kumamoto et al., 2016). Within the migratory $CD11b^+$ cDC2 gate, $CD9^-$ cells were $CD301b^-$ ($mCD301b^-$), whereas $CD9^+$ cells were found to be $CD301b^+$ ($mCD301b^+$) (Figure 1D and S1E). Due to the robustness of staining and parity with existing literature, CD301b was thus used for subsequent parsing of $CD11b^+$ cDC2 populations.

CD301b expression is often attributed to cells of monocyte/macrophage lineage and so we assessed expression of other monocyte/macrophage-related molecules on $mCD301b^-$ and $mCD301b^+$. While both $mCD301b^-$ and $mCD301b^+$ cells expressed CD135/FLT3 and

SIRPα, consistent with cDC2 assignment (Miller et al., 2012), mCD301b$^+$ expressed higher surface levels of markers generally associated with cells of a monocyte/macrophage lineage (Gautier et al., 2012), including CD14 (which we find later useful for parsing human cDC2 populations), CD16/32 (FcgRIII/II), CD200R and CD206 (Figure S1F). Furthermore, mCD301b$^+$ expressed higher levels of inhibitory receptors PD-L2 and LILRB4 (Figure S1G). Despite some of these markers being associated with cells of macrophage lineage, CD11b$^+$ cDC2 are phenotypically DC, based on expression of *Zbtb46* (Meredith et al., 2012; Satpathy et al., 2012) (Figure S1H).

With the assistance of unbiased scRNA-seq on bulk myeloid cells from the tdLN, we were able to derive a flow cytometry panel that encompasses this heterogeneity (Figure 1E) and determined the frequency of these populations (Figure S1I). With this comprehensive delineation of major myeloid populations within the tdLN, we next sought to identify the exact APC(s) responsible for anti-tumor CD4$^+$ T_{conv} priming by using the markers to track, isolate or genetically deplete distinct populations.

Requisite Migration of tdLN Populations

Previous work has highlighted the importance of CD103$^+$ cDC1 migration to the tdLN for productive antitumor CD8$^+$ T cell responses (Roberts et al., 2016). Less is known, however, about CD11b$^+$ cDC2 migration from the tumor and we sought to identify whether these two cDC2 populations were tumor-originating and tumor-antigen bearing. Consistent with our scRNA-seq analysis, populations identified as migratory were found to express surface CCR7 within the tdLN (Figure S1J), consistent with previous migration from a peripheral tissue.

We then assessed the levels of tumor antigen within myeloid cells of tdLN from B16-ZsGreen (B16^{ZsGr}) tumor-bearing animals (Figure 1F) and found that mCD103$^+$, mCD301b$^-$ and mCD301b$^+$ were the most dominant ZsGreen$^+$ migratory populations, while resident populations generally had lower and heterogeneous levels of uptake, consistent with previous findings (Roberts et al., 2016). Notably, CD301b$^-$ and CD301b$^+$ cDC2 are also present within the TME with fractions of both populations expressing CCR7 (Figure S1K), indicating their migratory capacity and providing confirmation of the abundant ZsGreen tumor antigen detected in these populations within the tdLN. We then generated B16-mCherry-OVA (B16^{ChOVA}) tumor-bearing *Ccr7−/−* mice, and confirmed that these lacked normal frequencies of all migratory DC in the tdLN (Figure S2A). Furthermore, in this context, adoptively transferred CD4$^+$ OT-II T cells were nearly completely unable to initiate proliferation (Figure S2B). This confirmed that migratory DC populations were critical but did not identify which cell population(s) could directly present antigens to drive proliferation nor how these populations would induce CD4$^+$ T_{conv} differentiation.

De novo priming of CD4$^+$ T_{conv} by cDC2 in the tdLN

Using mice bearing B16^{ChOVA} tumors, we sorted each of the identified tdLN myeloid populations, each of which contained *in vivo* acquired and processed tumor antigen, and co-cultured them *ex vivo* with naïve CD4$^+$ OT-II T cells. This demonstrated that migratory CD11b$^+$ cDC2, whether they be mCD301b$^-$ or mCD301b$^+$, supported CD4$^+$ OT-II T cell

expansion based on absolute cell number (Figure 2A) and frequency of cells undergoing cell division (Figure 2B). Importantly, despite similar antigen loading (Figure 1F), rCD11b$^+$ induced little proliferation of OT-II cells. Addition of exogenous OT-II OVA peptide ($OVA_{323–339}$) resulted in comparable activation and proliferation across myeloid populations, indicating that other populations are viable and otherwise capable of engaging CD4$^+$ T_{conv}, but likely simply do not process and present tumor antigen on MHC-II, restricting their ability to prime CD4$^+$ T_{conv} (Figure 2C, 2D).

To extend this study *in vivo,* we next tested whether CD11b$^+$ cDC2 were required for initiating CD4$^+$ T_{conv} priming within the tdLN. Mice lacking *Irf4* in DC have been shown to lack LN cDC2 (Krishnaswamy et al., 2017), however use of $Irf4^{flox/flox}Itgax^{Cre}$ resulted in consistent spontaneous germline deficiency (data not shown), complicating our efforts to delete *Irf4* specifically in the myeloid compartment. We instead used globally deficient $Irf4^{\Delta/\Delta}$ $(Irf4^{flox/flox}ActB^{Cre})$ $B16^{ChOVA}$-tumor-bearing animals, with adoptively transferred wild-type OT-II T cells, wherein we observed a reduction of all migratory cDC2 populations in the tdLN (Figure 2E). Transferred OT-II cells in $Irf4^{\Delta/\Delta}$ *mice* failed to proliferate as assessed by dye dilution and similarly failed to accumulate in the tdLN (Figure 2F). In contrast, in $Xcr1^{DTR}$ mice, depletion of mCD103$^+$ and rCD8α$^+$ did not impact OT-II proliferation (Figure S2C, S2D). By exploiting differential expression of *Cx3cr1* in rCD11b$^+$ (Supplemental Table 2), we generated $Cx3cr1^{lsl\text{-}DTR}CD11c^{Cre}$ animals that allowed for specific depletion of rCD11b$^+$ following DT administration (Figure S2E). Consistent with our *in vitro* findings, depletion of rCD11b$^+$ did not reduce OT-II proliferation (Figure S2F). Both *in vitro and in vivo,* migratory CD11b$^+$ cDC2, but not other cDC populations, were found to be the primary inducers of antitumoral CD4$^+$ T_{conv} priming.

Tolerogenic CD4$^+$ T_{conv} priming in the tdLN

In our tumor-bearing mice, effective anti-tumor immunity is not occurring despite evident initiation of CD4$^+$ T_{conv} priming and we hypothesized that CD4$^+$ T_{conv} differentiation by the identified cDC2 might not be generating effector differentiation. To examine this, we directly compared *in vivo* activation and differentiation of adoptively transferred OT-II T cells in the context of anti-tumor priming ($tdLN^{B16ChOVA}$) with tolerance-inducing priming via injection of adjuvant-free antigen (endoOVA) and with robust effector CD4$^+$ T_{conv} priming via infection by an influenza virus ($X31^{pOVA}$). We found that CD69 expression on OT-II at day 3, representing a marker of the strength of T cell activation (Allison et al., 2016) and/or exposure to inflammatory cytokines (Shiow et al., 2006; Sun et al., 1998), was similar in $tdLN^{B16ChOVA}$ and tolerizing endoOVA and much lower as compared to inflammatory priming with $X31^{pOVA}$ (Figure 2G). Correspondingly, other markers of activation observed in robust $X31^{pOVA}$ activation, namely CD44 upregulation and CD62L downregulation, were not observed to the same extent on the $tdLN^{B16ChOVA}$ OT-II T cells, which were largely similar to those primed by endoOVA (Figure 2H, 2I).

Finally, we found minimal downstream differentiation toward a protective ICOS$^+$ PD-1^{lo} T_h1 surface phenotype in both $tdLN^{B16ChOVA}$ and endoOVA conditions when examined day 7 post-transfer, compared to $X31^{pOVA}$ (Figure 2J). This also coincided with little to no cytokine production, notably IFNγ, following restimulation (Figure 2K). While we found

that cDC2 initiate $CD4^+$ T_{conv} priming in the tdLN, such defective effector T_{conv} differentiation predicts that therapeutic improvement of $CD4^+$ T_{conv} priming might either function through alterations in cDC2 phenotype, or via the licensing of other cell types to become APCs for $CD4^+$ T_{conv}.

Concommittant expansion of T_{reg} and $CD11b^+$ cDC2 in the TME

While examining the expansion of cDC2 in the TME of tumors with variable proportions of tumor cells secreting GM-CSF ($B16^{Gm\text{-}csf}$) (Broz et al., 2014), we found the surprising result that $CD4^+$ T_{conv} numbers did not rise appreciably with the induced increase in $CD11b^+$ cDC2 (considering both $CD301b^-$ and $CD301b^+$ cDC2 subsets) (Figure 3A, S3A). Given that these populations clearly express epitopes on MHC-II to $CD4^+$ T cells (Figure 2), we hypothesized that T_{reg} may prefentially expand in response to $CD11b^+$ cDC2 and may act as a feedback mechanism to suppress $CD11b^+$ cDC2 function and thus effective antitumor $CD4^+$ T_{conv} priming. Analyzing the same mice for T_{reg} proportion we found, indeed, a positive correlation between T_{reg} frequencies in the TME and cDC2 number. Given previous data suggesting that general DC may be altered or deleted by T_{reg} (Bauer et al., 2014), we sought to test whether T_{reg} might be restricting the trafficking and/or phenotype of $CD11b^+$ cDC2, thereby generating poorly differentiated $CD4^+$ T_{conv}.

Therapeutic benefits of T_{reg} depletion rely on *de novo* $CD4^+$ T_{conv} priming

Diptheria Toxin treatment of *Foxp3*^{DTR} mice (Kim et al., 2007) led to robust acute T_{reg} depletion and potent tumor rejection (Figure 3B and S3B, S3C) which required $CD4^+$ T_{conv} as previously described (Bos et al., 2013) (Figure 3C). To examine the role of tdLN $CD4^+$ T_{conv} priming specifically, we tested whether rejection depended on reactivation of $CD4^+$ T_{conv} already present in the TME or expansion and infiltration of recently activated $CD4^+$ T_{conv}. For this, we employed the use of the S1PR antagonist, FTY720, to block $CD4^+$ T_{conv} egress from the tdLN (Chiba et al., 1998). While FTY720 treatment had little effect on tumor growth in progressing tumors, FTY720/DT-treated *Foxp3*^{DTR} mice were unable to reject tumors in contrast to their DT-treated *Foxp3*^{DTR} controls (Figure 3D), demonstrating $CD4^+$ T_{conv} tdLN priming and egress is required for tumor rejection following T_{reg} depletion.

T_{reg} depletion induces enhancement of both $CD11b^+$ cDC2 and $CD4^+$ T_{conv}

Transfer of $CD4^+$ OT-II into $B16^{ChOVA}$ tumor-bearing T_{reg}-depleted animals led to greatly enhanced proliferation and expansion of OT-II in the tdLN at day 3 post-transfer compared to control (Figure 3E). Enhanced $CD4^+$ T_{conv} proliferation led us to hypothesize that T_{reg} depletion relieved suppression of the $CD11b^+$ cDC2/$CD4^+$ T_{conv} axis in the TME and tdLN. To test this, we first examined DC antigen trafficking to the tdLN following T_{reg} depletion in $B16^{ZsGr}$ tumor-bearing control and *Foxp3*^{DTR} mice. Following T_{reg} depletion, $ZsGreen^+$ $mCD301b^-$ and $mCD301b^+$ were greatly increased in absolute number in the tdLN, while other migratory populations were only weakly increased or unchanged (Figure 3F). We found that T_{reg}-mediated suppression of $CD11b^{\pm}$ cDC2 trafficking was not mediated through *Il-10, Itgb8* (Tgfb1-related) nor *Area* as knockout of these genes had no impact on the number of $ZsGreen^{\pm}$ $CD11b^{\pm}$ cDC2 in the tdLN (Figure S4A–S4C). Trafficking of these cells, however, depended upon chemokine-mediated tumor to tdLN trafficking as treating

mice with pertussis toxin (PTX), which blocks Gai signaling, blocked the rise in cDC2 in the T_{reg} deplete condition to a similar degree as the non-depleted controls (Figure S3D). Furthermore, we observed neither an increase in proliferation of CD11b$^{\pm}$ cDC2 in the tdLN (Figure S3E) nor profound changes in DC precursors in the bone marrow of *Foxp3^{DTR}* mice (Figure S3F,S3G), suggesting the expansion of CD11b$^{\pm}$ cDC2 was due to enhanced migration and not *in situ* proliferation in the tdLN or increased generation of DC. By analyzing changes in the abundance of CD11b^{+} cDC2 in the tdLN over time following T_{reg} depletion (Figure 3G), we were also able to determine that the wave of enhanced CD11b^{+} cDC2 migration temporally coincided with increases in the poorly-upregulated activation markers identified in Figure 2 (CD69 and CD44) (Figure 3H, S3H) consistent with a model in which a new wave of CD11b^{+} cDC2 carried the capacity to improve the quality of priming.

In order to test whether APC populations that trafficked to the tdLN in the absence of T_{reg} were capable of priming CD4^{+} T_{conv}, we co-cultured each APC isolated from *Foxp3^{DTR}* tdLN with CD4^{+} OT-II *in vitro* and measured their proliferation. This demonstrated that mCD301b^{-} and mCD301b^{+} remained the only cells capable of supporting T cell division and accumulation (Figure 4A, 4B), while other cells were still only able to prime CD4 T cells if provided exogenous antigen (Figure S5A). Furthermore, by crossing *Xcr1^{DTR}* with *Foxp3^{DTR}*, we were able to genetically exclude that neither mCD103^{+} nor rCD8α^{+} were now required for improved CD4^{+} T_{conv} priming and tumor rejection following T_{reg} depletion (Fig S5B–S5D).

To then determine whether CD11b^{+} cDC2 generated in the absence of T_{reg}, enhanced the quality of the priming reaction, we measured augmentation of CD69 expression on divided OT-II co-cultured with CD11b^{+} cDC2 *in vitro* (Figure 4C), and on divided OT-II transferred *in vivo* (Figure S5E). In both settings we found that, similar to CD4^{+} T_{conv} response in influenza (Figure 2), primed OT-II exhibited increased expression of CD69 compared to control tdLN conditions.

To directly measure the change in phenotype of CD11b^{+} cDC2 in the absence of T_{reg}, we examined transcriptional changes in bulk myeloid cells from *Foxp3^{DTR}* tdLN with scRNA-seq. This confirmed normal representation of myeloid populations within the *Foxp3^{DTR}* tdLN (Figure S5F) and comparable UMI within each cluster (Figure S5G). We first compared gene expression differences between mCD301b^{-} and mCD301b$^{\pm}$ from tdLN of Foxp3DTR mice and found that mCD301b^{-} expressed higher levels of costimulatory molecules (e.g. *Cd40, Cd70, Cd86)* in addition to key CD4$^{\pm}$ T_{conv} chemoattractant chemokines (e.g. *Ccl17, Ccl22),* while mCD301b$^{\pm}$ expressed higher levels of AP-1 family members (e.g. *Jun, Fos, Junb)* (Figure S5H **and** Supplemental Table 5A). We then aggregated scRNA-seq from tdLN and *Foxp3^{DTR}*tdLN data and performed DE analysis on mCD301b^{-} and mCD301b^{+} from the two conditions and found pronounced increases in costimulatory genes (*Cd80*, *Cd86*), genes involved in T cell chemoattraction *(Ccl17, Ccl22)* and genes expressed in response to pro-inflammatory cytokines *(Stati, Stat4)* on CD11b^{+} cDC2 in *Foxp3^{DTR}* tdLN (Figure 4D and Supplementary Table 5A). The increase in expression of both *Cd80* and *Cd86* was also verified by flow cytometry (Figure 4E),

although we found costimulatory levels to also be increased on other DC populations (Figure S5I).

We next assessed whether enhanced CD11b^{+} cDC2 functionality coincided with improved CD4^{+} T cell differentiation *in vivo.* We observed profound increases in CD44^{+} ICOS^{+} PD-1^{lo} T_h1-like cells in the tdLN and tumor following T_{reg} depletion, similar to the cells found following X31^{pOVA} (Figure 2, Figure 4F,4G). Importantly, we observed that these cells expressed T-bet, which is required for T_h1 differentiation (Figure S4J). However, loss of expression of the canonical cytokines in T_{reg}, namely *Il-10, Itgb8* (involved in processing of TGF-β1) or *Area,* had minimal impact on the proportion of ICOS$^{\pm}$ PD-1^{lo} T_h1-like cells in the tdLN (Figure S4A–S4C), suggesting T_{reg} utilize another mechanism to suppress the CD11b$^{\pm}$ cDC2/CD4$^{\pm}$ T_{conv} axis.

To confim that the increase in Th1-like cells in the tumor was due to enhanced *de novo* priming and differentiation, we again treated tumor-bearing control and *Foxp3^{DTR}* mice with DT and FTY720 and analyzed immune composition in both tdLN and TME. In the tdLN, FTY720 treatment had minimal impact in control mice but led to significant increases of T_h1-like cells in *Foxp3^{DTR}* tdLN (Figure 4H). In contrast, the proportion of T_h1-like CD4^{+} T_{conv} dropped precipitously in the TME of *Foxp3^{DTR}* mice following FTY720 treatment (Figure 4I), indicating that the increased T_h1-like CD4^{+} T_{conv} observed in the TME was due to enhanced *de novo* priming and subsequent tumor infiltration.

Anti-CTLA-4 based therapies function to induce expansion and functional enhancement of CD11b^{+} cDC2

Based our data in Figures 3 and 4, we hypothesized that T_{reg} depletion within the TME, more than systemic effects associated with systemic depletion, was critical for optimal enhancement CD11b^{+} cDC2 migration and enhanced CD4^{+} T_{conv} differentiation. To address this we tested various effector forms of anti-CTLA-4, either those that only blocked CTLA-4 or a form that also resulted in intratumoal T_{reg} depletion (cite Selby MS). Treatment of B16^{ZsGreen} tumor-bearing animals with a depleting anti-CTLA-4 clone (mouse IgG2c, clone: 9D9) led to a reduction of T_{reg} within the TME but not the tdLN (Figure 5A), and corresponded to increased migration of mCD301b^{+} to the tdLN, as compared to isotype (Figure 5B). This treatment elicited a significant increase in the proportion of ICOS^{+} PD-1^{lo} CD4^{+} T_{conv} in the tdLN and tumor (Figure 5C), similar to that seen in the *Foxp3^{DTR}* model (Figure 4). To assess whether these effects were due to T_{reg} depletion and not merely blockade of CTLA-4, we compared treatment with a non-depleting anti-CTLA-4 clone (mouse IgG1, clone: 9D9) and found, here, that T_{reg} were unchanged in the TME and tdLN, migration of either CD11 b^{+} cDC2 subset was unchanged and there was not an induction of ICOS^{+} PD-1^{lo} CD4^{+} T_{conv} in the tdLN and tumor (Supplemental Figure 6A–C). Furthermore, levels of costimulatory molecules CD80 and CD86 were only increased on mCD301b^{-} and mCD301b^{+} upon depletion of T_{reg} within the TME (Supplemental Figure 6D,E). Together these data strongly support that T_{reg} depletion in the TME is a primary driver of cDC2 migration and functional enhancement.

As we found GM-CSF can induce CD11b^{+} cDC2 expansion, we hypothesized that combination GVAX (irradiated B16$^{Gm\text{-}csf}$) and anti-CTLA-4 therapy potentiates CD4^{+} T_{conv}

immunity through concurrent expansion of CD11b$^+$ cDC2 and release of their suppression through T_{reg} depletion at the vaccine site. To assess this, we compared the immune composition of the vaccine site between BVAX (irradiated B16-F10) +/− anti-CTLA-4 and GVAX +/− anti-CTLA-4 (clone 9H10). In either GVAX condition, we observed significant increases of both CD11b$^+$ cDC2 subsets (Figure 5D), but anti-CTLA-4 treatment led to a reduction in T_{reg} and expansion of CD4$^+$ T_{conv}. (Figure 5E). We found that GVAX/anti-CTLA-4 functionally enhances CD11b$^+$ cDC2 as expression of both CD80 and CD86 on mCD301b$^-$ within the vaccine-draining LN (vaxLN) were most improved following combination GVAX/anti-CTLA-4, whereas mCD301b$^+$ benefitted primarily from GVAX alone (Figure 5F), indicating that perhaps T_{reg} more specifically suppress CD301b$^-$ cDC2. When we compared tumor growth between BVAX +/− anti-CTLA-4 and GVAX +/− anti-CTLA-4 we observed that BVAX alone or in combination with anti-CTLA-4 was ineffective at inducing robust antitumor immunity. In contrast, GVAX combined with anti-CTLA-4 lead to a reduction in tumor growth rates during the course of the experiment (Figure 5G). To assess CD11b$^+$ cDC2 depedency for CD4$^+$ T_{conv} priming against tumor vaccine antigen, we analyzed cDC composition in the vaccine site and vaxLN of control and *Irf4*$^{\Delta/\Delta}$ mice treated with anti-CTLA-4 and a combination of GVAX and irradiated B16^{ChOVA}. Similar to tumor-bearing animals, loss of *Irf4* greatly reduced the presence of CD11b$^+$ cDC2 in either site (Figure 5H), which corresponded to a near complete loss of CD4$^+$ OT-II proliferation in the vaxLN (Figure 5I). Taken together, these data along with our prior findings indicate that CD11b$^+$ cDC2 are active targets of T_{reg}-mediated suppression and are central to the initiation of CD4$^+$ T_{conv} antitumor immunity following therapeutic intervention.

scRNA-seq of the human tdLN reveals similar heterogeneity within cDC2 subset between mouse and human.

Recent scRNA-seq on normal human blood has highlighted heterogeneity within human cDC2 (here defined by CD1c$^+$/BDCA-1$^+$) (Villani et al., 2017), although the existence of these populations within the human tdLN has not been assessed in an unbiased manner. To determine whether human tdLN had similar populations and heterogeneity to that of mouse and human blood, we performed scRNA-seq on myeloid populations isolated from a patient's melanoma-draining LN. Following removal of non-APC cellular contaminants, we observed 7 unique clusters from 1,710 input cells (Figure 6A). Using DE and gene overlays, we were able to establish expressing cDC1 (hereby referred to as BDCA-3$^+$ cDC1) occupied cluster 5 and CD1C expressing cDC2 (hereby referred to as BDCA-1$^+$ cDC2) occupied cluster 0. The panel of genes expressed on cluster 0 and 5 were very similar to those identified previously for BDCA-1$^+$ cDC2 and BDCA-3$^+$ cDC1 (Villani et al., 2017), respectively, serving as confirmation of our initial identification (Figure 6B, 6C, Supplementary Table 6). To assess additional hetereogeneity within BDCA-1$^+$ cDC2, we reclustered BDCA-1$^+$ cDC2/cluster 0 and identified 3 populations (Figure 6D) that were transcriptionally distinct based on DE analysis (Figure 6E, 6F and Supplementary Table 7). Cluster 0.2 expressed high levels of CD1E, SLAMF7 and HLA-DQB2, genes that had been identified on a subset of blood cDC2 previously (Villani et al., 2017). Cluster 0.3, similar to mCD301b$^+$ cDC2 in mouse, expressed genes often associated with cells of a monocyte/macrophage lineage, including CD14, VCAN and S100A8 and like cluster 0.2, resembled a previously identified cDC2 population (Villani et al., 2017). Cluster 0.1 was unique in that it

was enriched for genes associated with cell motility (CORO1A, CRIP1, SEPT6, ANXA6) and may represent cellular status opposed to a *bona fide* distinct cellular population. We found that in addition to their presence within the human tdLN, $CD14^{-}$ BDCA-1^{+} cDC2 and $CD14^{+}$ BDCA-1^{+} cDC2 were present within the TME of a human head and neck squamous cell carcinoma (HNSC) tumor and both expressed CCR7, indicating their migratory potential (Figure 6G). While previously identified in blood, our data suggest that cDC2 subsets in human tdLN or TME have similar characteristics to mouse cDC2 subsets, though it remains a possibility that further heterogeneity still exists within this compartment in humans, particularly across individuals.

Parsing the predictive nature of BDCA-1^{+} cDC2 in the human TME

The results of our mouse models have specific predictions about the functional outcomes based on intratumoral cellular abundance. Data from Figure 3 and Figure 5 predict that $CD4^{+}$ T_{conv} quantity and quality will vary with intatumoral cDC2 and T_{reg} density. To assess this, we obtained 32 primary tumors from the head and neck region, a tumor type known to be rich in T_{reg} (Mandal et al., 2016), and analyzed their immune composition with two independent flow cytometry panels (Figure 6G, S7A). In plots of BDCA-1^{+} cDC2 and T_{reg} frequencies, we found three distinct patient TME with varied abundance of BDCA-1^{+} cDC2 or T_{reg} (Figure 7A). As predicted from the mouse models, patient TME with low representation of BDCA-1^{+} cDC2 demonstrated the lowest level of $CD4^{+}$ T_{conv} infiltration (Figure 7B). Consistent with T_{reg} suppressing $CD4^{+}$ T_{conv} immunity through BDCA-1^{+} cDC2, patients that were BDCA-1^{+} $cDC2^{HIGH}/Treg^{LOW}$ had greater $CD4^{+}$ T_{conv} infiltration than patients with BDCA-1^{+} $cDC2^{HIGH}/T_{reg}^{HIGH}$. To ensure that differences in $CD4^{+}$ T_{conv} were not merely due to a proportional shift, we analyzed $CD8^{+}$ T cell frequencies which we found to vary independently to either T_{reg} or $CD4^{+}$ T_{conv} frequency (Figure S7B).

Beyond total numbers, our model predicts improvements in $ICOS^{+}$ $PD\text{-}1^{lo}CD4^{+}$ T_{conv} phenotype would align with specific densities of BDCA-1^{+} cDC2 and T_{reg}. Patients whose biopsies (TME) were low for both BDCA-1^{+} cDC2 and T_{reg} had $CD4^{+}$ T_{conv} that lacked ICOS but expressed high levels of PD-1 while $CD4^{+}$ T_{conv} from tumors with high BDCA-1^{+} cDC2 and high T_{reg} had high PD-1 as well, though expressed intermediate amounts of ICOS, perhaps reflective of cells previously reported (Zappasodi et al., 2018) (Figure 7C). In contrast, $CD4^{+}$ T_{conv} from TME with abundant BDCA-1^{+} DC and low T_{reg} frequencies had significantly higher surface expression of ICOS, paired with decreased PD-1 (Figure 7C, S7C, S7D). While cancer staging at the time of analysis was fairly similar across classes of TME (Figure 7D), progression-free survival was significantly better in patients whose TME had abundant BDCA-1^{+} cDC2 and low T_{reg} than either of the other two TME classes (Figure 7E). Together these data suggest that the content of immune infiltrate informs not only the quality of an immune response ($ICOS^{+}$ $PD\text{-}1^{lo}$ $CD4^{+}$ T_{conv}) but also the capacity of antitumor immunity (progression-free survival).

The presence of high BDCA-3^{+} cDC1 and NK cells within the melanoma (SKCM) TME has been described as a general prognostic indicator of anti-PD-1 responsiveness (Barry et al., 2018), presumably due to their profoundly better ability to prime $CD8^{+}$ T cells. However, in that study, we also identified patients with higher densities of $CD4^{+}$ T_{conv} amongst

responders and these did not have higher densities of cDC1. We reasoned that perhaps those responders were primed for $CD4^+$ T_{conv} immunity and that this might instead rely upon cDC2. To thus assess whether BDCA-1^+ cDC2 could also contribute to anti-PD-1 responsiveness, we re-gated flow cytometry data from patient biopsies to reflect the recent heterogeneity identified within BDCA-1^+ cDC2. The frequency of BDCA-3^+ cDC1 and BDCA-1^+ cDC2 (both $CD14^{-/+}$) of HLA-DR were plotted (Figure 7F). Non-responder TME were generally lower for DC of both subtypes (Figure S7E). Responder TME were then divided based on the abundance of either BDCA-3^+ cDC1 or BDCA-1^+ cDC2. We found that responders high for BDCA-1^+ cDC2, compared to responders high for BDCA-3^+ cDC1 had a significantly lower proportion of $CD8^+$ T cells but significantly higher $CD4^+$ T_{conv} within their TME (Figure 7G), promoting the hypothesis that these patients have improved $CD4^+$ T_{conv} activity even with lower overall $CD8^+$ T cell abundance. We reasoned that BDCA-1^+ cDC2 abundance alone may predict $CD4^+$ T_{conv} quantity in melanoma (SKCM), as proportions of T_{reg} were significantly lower than in HNSC. (Figure 7H). These data suggest that classes of human TME can be divided based on the abundance of BDCA-1^+ cDC2 and that this can be an indicator for both $CD4^+$ T_{conv} quality and represent patients likely to respond to ICB.

Discussion

Here, we define the cell type(s) necessary for *de novo* priming of new antitumor $CD4^+$ T_{conv}. A fundamental conclusion is that MHC-II presentation of peptides to prime naive $CD4^+$ T_{conv} is heavily biased to $CD11b^+$ cDC2, with the distinction between tumor control and tumor tolerance being determined by the phenotype of these cells. $CD4^+$ T_{conv} priming in tdLN most resembles that of non-inflamed lymph nodes, where $CD4^+$ T_{conv} are generated with a depressed activation state, with little or no evidence of the Th1 -like $ICOS^+$ PD-1^{lo} phenotype (Figure 2). While the TME may futher drive exhaustion, this conclusion suggests that efficacy of immunotherapies for $CD4^+$ T_{conv} will rely on modulation of this defective step of priming. Indeed, given the apparent irreversibility of certain forms of exhaustion (Philip et al., 2017), it is possible that the efficacy of ICB is linked to ongoing *de novo* lymph node priming rather than only blockade of checkpoint ligands in the tumor.

Our scRNA-seq and functional data demonstrate that two distinct populations of IRF4-dependent $CD11b^+$ cDC2 – for which we found homologs in human tdLN and TME – are required *in vivo* for initiating activation of antitumor $CD4^+$ T_{conv}. The complement of myeloid cells identified in mouse tdLN are consistent with previous reports (Ochiai et al., 2014; Salmon et al., 2016; Tussiwand et al., 2015), however, our approach assayed all populations in parallel allowing for unambiguous confirmation of $CD4^+$ T_{conv} stimulatory function. While our data suggest mCD301b^- and mCD301b^+ play largely redundant roles in antitumor immunity, as each population was capable of supporting comparable OT-II proliferation *ex vivo* and collectively *in vivo* (Figure 2), we cannot exclude the possibility that these cell populations have disparate functions in other tumor models or following different treatments. Following T_{reg} depletion, mCD301b^- displayed enhanced expression of both chemokines linked to $CD4^{\pm}$ T_{conv} chemoattraction and costimulatory molecules as compared to mCD301b_+ (Figure 4). Paired with our findings suggesting mCD301$b^{\pm}$ in tdLN express higher surface levels of inhibitory PD-L2 and LILRB4 (Figure 1), we postulate that

perhaps mCD301b$^-$ are more supportive of productive antitumor CD4$^{\pm}$ T_{conv} differentiation. cDC2 have been previously associated with CD4$^+$ T_{conv} priming, with CD301b$^+$ cDC2 being shown to specifically induce Th2 responses to adjuvant (Kumamoto et al., 2013) and a second report suggesting that pan-cDC2 population in tumor was demonstrated to induce T_h17 differentiation primarily *in vitro* (Laoui et al., 2016). However, our findings specifically document suboptimal triggering of early activation (e.g. CD69, CD44 levels) as well as poor induction of differentiation in OT-II from tdLN and non-inflammed LN compared to inflammatory conditions such as influenza or Treg-depletion (Figure 2). Previous work has identified an IFNγ-dependent homeostatic 200 gene program associated with poor DC:T cell priming, some of which are co-opted in tumors (Nirschl et al., 2017). We also found expression of some of these genes in tdLN mDC (e.g. *Socs2, Fscn1)* (Figure 1) and were able to further define a functional readout for phenotypic defects in CD11b$^+$ cDC2. Whether expression of these genes is associated with T_{reg}-mediated suppression or defects in CD4$^+$ T_{conv} differentiation is unclear, although these data support a homeostatic phenotypic dampening of cDC function, in particular cDC2, that can be reverted during specific inflammatory settings.

Both systemic and tumor-specific therapeutic depletion of T_{reg} enhanced cDC2 migration and reverted phenotypic dysfunction, which in turn allowed productive antitumor CD4$^+$ T_{conv} priming to occur in the tdLN. Previous studies have demonstrated reactivated CD4$^+$ T_{conv} immunity following T_{reg}-depletion (Bos et al., 2013; Wallin et al., 2016), although the mechanism and the prominence of cDC2 in modulating differentiation, through which reactivation occured was unclear. While systemic inflammation in response to global Treg depletion may provide added modulation of myeloid development, our data supports a central role of T_{reg}, largely at the tumor site, as critical modulators of cDC2. Although we cannot preclude the possibility that T_{reg} suppress CD4$^+$ T_{conv} directly (Pandiyan et al., 2007) or impact DC more generally (Bauer et al., 2014; Qureshi et al., 2011), our data demonstrates a potently immunosuppressive relationship between T_{reg} and CD11b$^+$ cDC2, although the specific means through which T_{reg} exert this suppression on cDC2 is still unknown (Supplemental Figure 5). Expansion of CD11b$^+$ cDC2, in either the TME (Figure 3) or GVAX site (Figure 5), induces concurrent increases in T_{reg} which likely represents that cDC2 produced under these conditions undergo continued suppression, opposing their ability to drive productive priming of effector CD4$^+$ T_{conv}. This is consistent with data from others showing T_{reg} require MHC-II on DC to expand in the periphery (Zou et al., 2010). Enhanced cDC2 migration to the tDLN was observed following T_{reg} depletion induced by either genetic or therapeutic means (Figure 3, Figure 4). While DC can upregulate CCR7 in response to inflammatory cues (Krappmann et al., 2004), DC can also migrate continuously under homeostatic conditions (Baratin et al., 2015). Given the rapid migration of of cDC2 from tumor to tdLN following Treg-depletion, we suspect that Treg may regulate homeostatic cDC2 trafficking to the tdLN.

Phenotypically enhanced CD11b$^+$ cDC2 were better able to support CD4$^+$ T_{conv} priming and support improved differentiation to a ICOS$^+$ PD-1^{lo} Th1-like phenotype (Figure 3, Figure 4). Although CD103$^+$ cDC1 have been shown to induce T_h1 immunity in specific inflammatory settings (Liang et al., 2016), they were dispensible for tumor rejection following T_{reg} depletion, supporting our data demonstrating that CD11b$^+$ cDC2 are uniquely able to initiate

productive antitumor $CD4^+$ T_{conv} priming in the absence of T_{reg} (Figure 4). Efficacious anti-CTLA-4 treatment in both mouse and human is associated with the generation of $ICOS^+$ $PD\text{-}1^{lo}$ T_h1-like systemically (Fan et al., 2014; Wei et al., 2017), although the site of this population's initial emergence was previously undefined. We found that antitumor $ICOS^+$ $PD\text{-}1^{lo}$ $CD4^+$ T_{conv} arise in tdLN during *de novo* priming and additionally that infiltration of these tdLN-derived antitumor $CD4^+$ T_{conv}, as opposed to via local reactivation in the TME, was the dominant mechanism through which tumor rejection occurred (Figure 3, Figure 4). While we did not directly assess this, we hypothesize that $CD4^{\pm}$ T_{conv} downregulate CD62L in a *Foxp3*^{DTR} tdLN, allowing for improved circulation and TME entry. Interestingly, $CD4^{\pm}$ T_{conv} as opposed to $CD8^{\pm}$ T cells were required for tumor rejection (Figure 3), although it is currently unclear whether $CD4^{\pm}$ T_{conv} are cytoxic themselves or induce other immune populations to participate in tumor cell elimination. Together, this highlights the importance of enhancing cDC2 phenotype in patients in order to improve distal priming for more effective immunotherapy.

In human HNSC TME, we found a remarkable concordance with our T_{reg} depletion data whereby heterogeneity in T_{reg} and cDC2 abundance parsed subsets of patients with distinct phenotypes and, in particular, the relationship between BDCA-1^+ cDC2 and T_{reg} informed both the quantity and character of $CD4^+$ T_{conv}. This parallel with our data in mouse strongly suggests that a similar mechanism of T_{reg}-mediated suppression exists in human. The use of T_{reg} alone as a prognostic indicator has varying levels of predictive power (Shang et al., 2015) and this may in part be due to the fact tha low T_{reg} abundance fails to differentiate cohorts that have or do not have requisite cDC2 populations for $CD4^+$ T_{conv} priming. Our pairing of T_{reg} abundance with the additional parameter (BDCA-1^+ cDC2) unmasks hetereogeneity of TME, allowing for significant predictions of immune response quality and disease-free survival (Figure 7). Looking forward, this suggests that BDCA-1^+ DC abundance is a biomarker for a primed microenvironment for response to ICB or to novel therapies targeting T_{reg} suppression of cDC2. Indeed, a human TME dataset of anti-PD-1 responder/non-responders demonstrated that while BDCA-3^+ cDC1 cellularity is largely associated with anti-PD-1 responsiveness (Barry et al., 2018), some patients were surprisingly BDCA-3^+ cDC1 low, but contained higher proportions of BDCA-1^+ cDC2 and $CD4^+$ T_{conv}, suggesting that at least in some TME, such as those with tumor cells that express MHC-II (Johnson et al., 2016), $CD4^+$ T_{conv} may be capable of playing a preeminent role in successful antitumor responses.

Taken together, our work highlights $CD11b^+$ cDC2/BDCA-1^+ cDC2 as a target of T_{reg} suppression and as a necessary population for directing antitumor $CD4^+$ T_{conv} immunity. Furthermore, cDC2 abundance in the human TME may act as a biomarker for not only $CD4^+$ T_{conv} quality but also as a contributing indicator for responsiveness to ICB. Classifying TME based on immune infiltrate has predictive power (Binnewies et al., 2018) and thus recent (Azizi et al., 2018; Lavin et al., 2017; Puram et al., 2017) and future efforts to characterize disparate TME with unbiased high-dimensional techniques will undoubtable prove invaluable for identifying unique classes of patient TME that are profoundly immunosuppressed or poised for therapeutic response.

Materials and Methods

Human Tumor Samples

The human head and neck tumor set consisted of a total of 32 tumors removed from the head and neck region, agnostic to location. The anti-PD-1 responder/non-responder melanoma tumor set was published previously (Barry et al., 2018). All patients consented for tissue collection under a UCSF IRB approved protocol (UCSF IRB# 13– 12246 and 14–15342). Samples were obtained after surgical excision with biopsies taken by the Pathology Department to confirm the presence of tumor cells. Patients were selected without regard to prior treatment. Freshly resected samples were placed in ice-cold PBS or Leibovitz's L-15 medium in a 50 mL conical tube and immediately transported to the laboratory for evaluation. Patient samples were coded and flow analysis was scored by separate individuals prior to data agglomeration. All samples were processed and analyzed by flow cytometry, but only those with at least 1,000 live $CD45^+$ cell events were included in the analysis.

Mice

All mice were treated in accordance with the regulatory standards of the National Institutes of Health and American Association of Laboratory Animal Care and were approved by the UCSF Institution of Animal Care and Use Committee. The following mice were purchased for acute use or maintained under specific pathogen-free conditions at the University of California, San Francisco Animal Barrier Facility. We attempted to use *Irf4*$^{flox/flox}$;*CD11c-Cre* but discovered independent breeding cages were producing germline *Irf4* globally deficient pups, complicating our findings (data not shown).

Method Details

Tumor cell lines, tumor cell injections and tumor growth experiments

B16-F10 (ATCC, CRL-6475) was purchased. B16-ChOVA (B16ChOVA), a derivative of B16-F10, was created through transduction of B16-F10 with an mCherry-OVA (ChOVA) fusion construct identical to that used in previous studies in our lab (Engelhardt et al., 2012; Roberts et al., 2016). $B78^{ChOVA}$, derived from the parental B78 subline of B16, was generated in our laboratory and described previously (Broz et al., 2014). B16-ZsGreen (B16ZsGr) was previously generated in our laboratory as described (Headley et al., 2016). B16GM-CSF (GVAX) (Dranoff et al., 1993) were acquired from the laboratory of Dr. Lawrence Fong at UC San Francisco. Adherent cell lines were cultured at 37°C in 5% CO_2 in DMEM (Invitrogen), 10% FCS (Benchmark), Pen/Strep/Glut (Invitrogen).

For tumor cell injection, adherent tumor cells were lifted using 0.05% Trypsin-EDTA (Thermo Fisher Scientific) and washed 3X with DPBS (Thermo Fisher Scientific). 1.0×10^5 – 2.5×10^5 tumor cells were resuspended in DPBS and mixed 1:1 with Matrigel GFR (Corning) for a final injection volume of 50 μL. Mice anesthetized with isoflurane (Henry Schein) were shaved on their flank and injected subcutaneously either unilaterally or bilaterally depending on the experimental setup.

For tumor measurements, tumors were typically measured 3 times per week using electronic calipers. Tumor volume was calculated through the formula $V = 0.5(w2 \times l)$. Mice were removed from the study and euthanized when tumors exceeded a volume of 1000 mm^3.

Single Cell RNA Sequencing (scRNA-Seq)

For mouse scRNA-seq, live $CD90.2^-$ $B220^-$ $Ly6G^-$ $NK1.1^-CD11b^+$ and/or $CD11c^+$ cells were sorted from inguinal and axillary LN with a BD FACSAria Fusion. For human scRNA-seq, live $CD3^-CD19/20^-CD56^-$ cells were sorted from a melanoma-draining LN on a BD FACSAria Fusion. After sorting, cells were pelleted and resuspended at 1×10^3 cells/μl in 0.04%BSA/PBA and loaded onto the Chromium Controller (10X Genomics). Samples were processed for single-cell encapsulation and cDNA library generation using the Chromium Single Cell 3' v2 Reagent Kits (10X Genomics). The library was subsequently sequenced on an Illumina HiSeq 4000 (Illumina).

Single Cell Data Processing

Sequencing data was processed using 10X Genomics Cell Ranger V1.2 pipeline. The Cell Ranger subroutine *mkfastq* converted raw, Illumina bcl files to fastqs which were then passed to Cell Ranger's *count,* which aligned all reads using the aligner STAR (Dobin et al., 2013) against UCSC mm10 or GRCh38 genomes for mouse and human cells, respectively. After filtering reads with redundant unique molecular identifiers (UMI), *count* generated a final gene-cellular barcode matrix. Both *mkfastq* and *count* were run with default parameters.

Cellular Identification and Clustering

For each sample, the gene - barcode matrix was passed to the R (v. 3.4.3) software package Seurat (Satija et al., 2015) (http://satijalab.org/seurat) (v2.3.0) for all downstream analyses. We then filtered on cells that expressed a minimum of 200 genes and required that all genes be expressed in at least 3 cells. We also removed cells that contained > 5% reads associated with cell cycle genes (Kowalczyk et al., 2015; Macosko et al., 2015). Count data was then log2 transformed and scaled using each cell's proportion of cell cycle genes as a nuisance factor (implemented in Seurat's *ScaleData* function) to correct for any remaining cell cycle effect in downstream clustering and differential expression analyses. For each sample, principal component (PC) analysis was performed on a set of highly variable genes defined by Seurat's *FindVariableGenes* function. Genes associated with the resulting PCs (chosen by visual inspection of scree plots) were then used for graph-based cluster identification and subsequent dimensionality reduction using t-distributed stochastic neighbor embedding (tSNE). Cluster-based marker identification and differential expression were performed using Seurat's *FindAllMarkers* for all between-cluster comparisons.

ImmGen Signature Generation

To generate *a priori* signatures for the myeloid cell types that we expected to find in the mouse tdLN sample, we downloaded microarray based transcriptional profiles from the Immunological Genome Project data Phase 1(Heng and Painter, 2008) (GSE15907). See Supplementary Table 1 for the specific samples used.

For each ImmGen population, we performed DE analysis comparing samples from the population of interest to the aggregate of the remaining 6 groups using the R package *limma* (Ritchie et al., 2015). We ordered the top 20 genes with the smallest FDR values (Benjamini and Hochberg, 1995) by fold change (excluding any genes that were downregulated in the group of interest) and then cross referenced the resulting list with the single cell expression matrix from each sample. This left genes that were both highly differentially expressed in the IMMGEN profiles and expressed in our single cell data sets of interest. The top 10 genes (or fewer if less than 10 genes remained) by fold change were then median normalized and aggregated to create a single "signature gene" for each cell type. These signature genes were 0–1 scaled and plotted in the context of the *t*-SNE dimensionality reduction to show cellular location.

Sequencing Sample Aggregation

In order to generate pairwise aggregations between samples and control for potential batch effects, we used Seurat's Canonical Correlation Analysis (CCA) functionality. All post-filtered cells from each of the single sample analyses were used in the aggregate. CCA was performed on the union of the 2000 genes with highest dispersions from each dataset. The number of canonical correlation vectors (CCVs) used in downstream clustering and *t*-SNE analyses was chosen by visual inspection of heatmaps of genes associated with those top CCVs. Results were robust to moderate changes in this final number of CCVs.

Mouse Tissue Digestion and Flow Staining

Tumor and LN tissues were harvested and enzymatically digested with 0.2 mg/ml DNAse I (Sigma-Aldrich), 100 U/ml Collagenase I (Worthington Biochemical), and 500 U/ml Collagenase Type IV (Worthington Biochemical) for 30–45 minutes at 37 °C. TdLN included inguinal and axillary LN. Tumor samples were subjected to consistent agitation during this time and LN samples were rapidly pipetted at the half-point time. Samples were filtered to generate a single-cell suspension and washed with stain media (PBS, 2% FCS). For bone marrow cells, mouse femurs and tibias were flushed with stain media and subsequently underwent red blood cell lysis.

Cells harvested from these tissues or *in vitro* culture were washed with PBS and stained with Zombie NIR fixable viability dye (BioLegend) for 30 minutes at 4°C to distinguish live and dead cells. Cells were then washed with stain media and non-specific binding was blocked with anti-CD16/32 (BioXCell), and 2% rat serum (Invitrogen) and 2% Armenian hamster serum (Innovative Research). Cell surface proteins were then stained on ice for 30 minutes. Cells were washed again and resuspended with stain media prior to collection and analysis on a BD Fortesssa or LSR-II flow cytometer. When applicable, black latex beads were added to the sample for quantification of absolute cell number. For intracellular stains, cells were fixed and permeabilized with the FoxP3/Transcription Factor Staining Buffer Set (Thermo Fisher Scientific) after surface marker staining. Intracellular antibodies were stained in permeabilization buffer with 2% rat serum for at least 30 minutes at room temperature.

Human Tissue Digestion and Flow Staining

Tumor or LN tissue was thoroughly chopped with surgical scissors and transferred to GentleMACs C Tubes (Miltenyi Biotec) containing 20 uL/mL Liberase TL (5 mg/ml, Roche) and 50 U/ml DNAse I (Roche) in RPMI 1640 per 0.3 g tissue. GentleMACs C Tubes were then installed onto the GentleMACs Octo Dissociator (Miltenyi Biotec) and incubated according to the manufacturer's instructions. Samples were then quenched with 10 mL of sort buffer (PBS/2% FCS/2mM EDTA), filtered through 100 um filters and spun down. Red blood cell lysis was performed with 175 mM ammonium chloride.

Cells were then incubated with Human FcX (Biolegend) to prevent non-specific antibody binding. Cells were then washed in DPBS and incubated with Zombie Aqua Fixable Viability Dye (Biolegend). Following viability dye, cells were washed with sort buffer and incubated with cell surface antibodies for 30 minutes on ice and subsequently fixed in either Fixation Buffer (BD Biosciences) or in Foxp3/Transcription Factor Staining Buffer Set (ThermoFisher Scientific) if intracellular staining was required.

APC-T cell *In Vitro* Co-Culture Assays

APC populations were double-sorted (yield followed by purity) from tdLN using a BD FACSAria Fusion and co-cultured with 2×104 isolated eFluor670-labeled OT-II T cells at a 1:5 ratio in complete RPMI (Pen/Strep, NEAA, NaPyr, 2-ME, 10% FCS) in 96-well V-bottom plates. Cells were harvested for analysis 3 days later. OVA peptide 323–339 (GenScript) was added to wells at 1 μg/ml as a positive control.

Mouse T cell Isolation and *In Vivo* Adoptive T Cell Transfer

Inguinal, axillary, brachial, superficial cervical and mesenteric LN were isolated from CD45.1$^+$ OT-II mice. LN were smashed through 100 um filters and subsequently spun down and counted. CD4$^+$ T cells were then isolated using EasySep CD4 negativeselection kits (STEMCELL Technologies).

1×10^5 isolated CD45.1$^+$ CD4$^+$ OT-II T cells were either transferred immediately in cases of PMA/Ionomycin restimulation experiments or labeled with Cell Proliferation Dye eFluor670 (Thermo Fisher Scientific) and 1.0–5.0×10^5 cells were adoptively transferred to CD45.2$^+$ mice. LN were harvested for proliferation analysis at day 3 posttransfer and for PMA/ionomycin re-stimulation at day 7 post-transfer. *XCR1^{DTR}* and *Cx3cr1iDTR* mice were treated with 500 ng of DT every other day beginning the day prior to OT-II transfer through the experimental end point. *Foxp3^{DTR}* mice were injected with DT for two days prior to OT-II transfer and then the day following OT-II transfer.

T Cell Cytokine Analysis

For cytokine analysis of endogenous or adoptively transferred T cells, cells from either LN or tumors were used for re-stimulation. Single cell suspensions were incubated with 50 ng/ml PMA (Sigma-Aldrich), 500 ng/ml ionomycin (Thermo Fisher Scientific), 3 μg/ml brefeldin A (Cayman Chemical Company), and 2μM monensin (Thermo Fisher Scientific) for 5–6 hours in complete RPMI and stained for surface and intracellular proteins using the Foxp3/Transcription Factor Staining Buffer Set (ThermoFisher Scientific).

In Vivo Treatments

For diphtheria toxin (DT), while treatment schedules varied depending upon mouse genetic strain or type of experiment, mice received 500 ng boluses of un-nicked DT (List Biologics, 150) intraperitoneally. *Foxp3*^{DTR}, *XCR1*^{DTR} and *Cx3cr1*^{iDTR} mice were typically injected on days 9, 10 and 12 followed by flow cytometric analysis at day 14.

For comparisons of CD4$^+$ T_{conv} priming between steady-state, tumor-bearing and influenza-infected conditions, mice were injected subcutaneously with either 20 μg of endotoxin-free ovalbumin (Invivogen) in 50 μl of PBS or 2.0×10^5 B16ChOVA. Mice receiving influenza were infected intranasally with 1×10^5 PFU of X31-OT-II (Thomas et al., 2006), prepared as previously described (GeurtsvanKessel et al., 2008).CD45.1$^+$ OT-II$^+$ CD4$^+$ T cells were transferred intravenously 2 days after ovalbumin and X31-OT-II treatment and 14 days after B16^{ChOVA} injection.

To assess CD4/CD8 T cell dependency for tumor rejection following T_{reg} depletion or GVAX/anti-CTLA-4 treatment, mice were injected with 250 μg of isotype (Clone: LTF-2, BioXCell), anti-CD4 (Clone: GK1.5, BioXCell) or anti-CD8a (Clone: 2.43, BioXCell) was injected at days 10, 13 and 16 post-tumor injection for *Foxp3*^{DTR} and days 4, 7 and 10 for GVAX/anti-CTLA-4 treatment.

To assess the requirement of T cell LN egress, control or *Foxp3DTR* mice were treated with 500 ng of DT on days 9, 10 and 12 post-tumor injection and with 200 μg FTY720 (Cayman Chemicals) every day beginning on day 8 post-tumor injection through the end of the experiment.

For Fc-modified anti-CTLA-4 experiments, mice were injected with 2×10^5 B16^{ZsGreen} cells. On days 7, 9, 10, 11 and 13 post-tumor injection, mice received 250 μg of mouse IgG2c isotype, anti-CTLA-4 IgG2c (modified clone 9D9, Bristol-Myers-Squibb), mouse IgG1 isotype or anti-CTLA-4 IgG1 (modified clone 9D9, Bristol-Myers-Squibb).

For GVAX/anti-CTLA-4 experiments, mice were injected with either 1×10^5 (tumor growth) or 2×10^5 B16-F10 (cellular analysis). On days 3, 6 and 9 post-tumor injection, mice were injected subcutaneously on their contralateral flank with either PBS or 1×10^6 50 Gy-irradiated GVAX cells and received either 250 μg anti-CTLA-4 (9H10, BioXCell) or Syrian hamster IgG isotype (BioXcell) on day 3, and 100 μg of antibody on days 6 and 9.

Statistical analysis and experimental design

Unless specifically noted, data displayed is from a representative experiment of ≥ 2 independent experiments. Experimental group assignment was determined by genotype or, if all wild-type mice, by random designation. Error bars represent mean ± S.E.M. calculated using Prism unless otherwise noted. Statistical analyses were performed using GraphPad Prism software. For pairwise comparisons, unpaired T tests were used unless otherwise noted. For statistical measures between more than two groups, one-way ANOVA would be performed unless otherwise noted. Comparisons found to be nonsignificant are not shown. Investigators were not blinded to group assignment during experimental procedures or analysis.

Supplementary Material

Refer to Web version on PubMed Central for supplementary material.

Acknowledgements

We thank E. Wan in the Institute for Human Genetics at UCSF for helping prepare samples for single-cell RNA-sequencing. We would also like to thank the UCSF Parnassus Flow Cytometry Core for maintenance of flow cytometers and sorters. J.J. Engelhardt and Bristol-Myers-Squibb for Fc-modified anti-CTLA-4 antibodies. S.M. Kaech, M. Conti, and M.D. Rosenblum for various mouse strains. L. Rodda for advice related to single-cell RNA sequencing and M.L. Broz and M.B. Headley for guidance, advice and critical reading of the manuscript. Acquisition and analysis of certain human samples described in this study was partially funded by contributions from AbbVie, Amgen, Bristol-Myers Squibb, and Pfizer. This work was supported in part by the NSF Graduate Research Fellowship Program awarded to M.B and NIH grants U54 CA163123, R21CA191428 and R01 CA197363.

References

Alferink J, Lieberam I, Reindl W, Behrens A, Weiss S, Huser N, Gerauer K, Ross R, Reske-Kunz AB, Ahmad-Nejad P, et al. (2003). Compartmentalized production of CCL17 in vivo: strong inducibility in peripheral dendritic cells contrasts selective absence from the spleen. The Journal of experimental medicine 197, 585–599. [PubMed: 12615900]

Allison KA, Sajti E, Collier JG, Gosselin D, Troutman TD, Stone EL, Hedrick SM, and Glass CK (2016). Affinity and dose of TCR engagement yield proportional enhancer and gene activity in CD4+ T cells. eLife 5.

Azizi E, Carr AJ, Plitas G, Cornish AE, Konopacki C, Prabhakaran S, Nainys J, Wu K, Kiseliovas V, Setty M, et al. (2018). Single-Cell Map of Diverse Immune Phenotypes in the Breast Tumor Microenvironment. Cell.

Baratin M, Foray C, Demaria O, Habbeddine M, Pollet E, Maurizio J, Verthuy C, Davanture S, Azukizawa H, Flores-Langarica A, et al. (2015). Homeostatic NF-kappaB Signaling in Steady-State Migratory Dendritic Cells Regulates Immune Homeostasis and Tolerance. Immunity 42, 627–639. [PubMed: 25862089]

Baratin M, Simon L, Jorquera A, Ghigo C, Dembele D, Nowak J, Gentek R, Wienert S, Klauschen F, Malissen B, et al. (2017). T Cell Zone Resident Macrophages Silently Dispose of Apoptotic Cells in the Lymph Node. Immunity 47, 349–362.e345. [PubMed: 28801233]

Barry KC, Hsu J, Broz ML, Cueto FJ, Binnewies M, Combes AJ, Nelson AE, Loo K, Kumar R, Rosenblum MD, et al. (2018). A natural killer-dendritic cell axis defines checkpoint therapy-responsive tumor microenvironments. Nature medicine.

Bauer CA, Kim EY, Marangoni F, Carrizosa E, Claudio NM, and Mempel TR (2014). Dynamic Treg interactions with intratumoral APCs promote local CTL dysfunction. The Journal of clinical investigation 124, 2425–2440. [PubMed: 24812664]

Bedoui S, Whitney PG, Waithman J, Eidsmo L, Wakim L, Caminschi I, Allan RS, Wojtasiak M, Shortman K, Carbone FR, et al. (2009). Cross-presentation of viral and self antigens by skin-derived CD103+ dendritic cells. Nat Immunol 10, 488–495. [PubMed: 19349986]

Behrens G, Li M, Smith CM, Belz GT, Mintern J, Carbone FR, and Heath WR (2004). Helper T cells, dendritic cells and CTL Immunity. Immunology and cell biology 82, 84–90. [PubMed: 14984599]

Belz GT, Shortman K, Bevan MJ, and Heath WR (2005). CD8alpha+ dendritic cells selectively present MHC class I-restricted noncytolytic viral and intracellular bacterial antigens in vivo. Journal of immunology (Baltimore, Md : 1950) 175, 196–200.

Binnewies M, Roberts EW, Kersten K, Chan V, Fearon DF, Merad M, Coussens LM, Gabrilovich DI, Ostrand-Rosenberg S, Hedrick CC, et al. (2018). Understanding the tumor immune microenvironment (TIME) for effective therapy. Nature medicine 24, 541–550.

Bos PD, Plitas G, Rudra D, Lee SY, and Rudensky AY (2013). Transient regulatory T cell ablation deters oncogene-driven breast cancer and enhances radiotherapy. The Journal of experimental medicine 210, 2435–2466. [PubMed: 24127486]

Broz ML, Binnewies M, Boldajipour B, Nelson AE, Pollack JL, Erle DJ, Barczak A, Rosenblum MD, Daud A, Barber DL, et al. (2014). Dissecting the tumor myeloid compartment reveals rare activating antigen-presenting cells critical for T cell immunity. Cancer Cell 26, 638–652. [PubMed: 25446897]

Chen DS, and Mellman I. (2013). Oncology meets immunology: the cancer-immunity cycle. Immunity 39, 1–10. [PubMed: 23890059]

Chiba K, Yanagawa Y, Masubuchi Y, Kataoka H, Kawaguchi T, Ohtsuki M, and Hoshino Y. (1998). FTY720, a novel immunosuppressant, induces sequestration of circulating mature lymphocytes by acceleration of lymphocyte homing in rats. I. FTY720 selectively decreases the number of circulating mature lymphocytes by acceleration of lymphocyte homing. Journal of immunology (Baltimore, Md : 1950) 160, 5037–5044.

Corthay A, Skovseth DK, Lundin KU, Rosjo E, Omholt H, Hofgaard PO, Haraldsen G, and Bogen B. (2005). Primary antitumor immune response mediated by CD4+ T cells. Immunity 22, 371–383. [PubMed: 15780993]

Curran MA, Geiger TL, Montalvo W, Kim M, Reiner SL, Al-Shamkhani A, Sun JC, and Allison JP (2013). Systemic 4–1BB activation induces a novel T cell phenotype driven by high expression of Eomesodermin. The Journal of experimental medicine 210, 743–755. [PubMed: 23547098]

Fan X, Quezada SA, Sepulveda MA, Sharma P, and Allison JP (2014). Engagement of the ICOS pathway markedly enhances efficacy of CTLA-4 blockade in cancer immunotherapy. The Journal of experimental medicine 211, 715–725. [PubMed: 24687957]

Gao Y, Nish SA, Jiang R, Hou L, Licona-Limon P, Weinstein JS, Zhao H, and Medzhitov R. (2013). Control of T helper 2 responses by transcription factor IRF4-dependent dendritic cells. Immunity 39, 722–732. [PubMed: 24076050]

Gautier EL, Shay T, Miller J, Greter M, Jakubzick C, Ivanov S, Helft J, Chow A, Elpek KG, Gordonov S, et al. (2012). Gene-expression profiles and transcriptional regulatory pathways that underlie the identity and diversity of mouse tissue macrophages. Nat Immunol 13, 1118–1128. [PubMed: 23023392]

Gerner MY, Casey KA, Kastenmuller W, and Germain RN (2017). Dendritic cell and antigen dispersal landscapes regulate T cell immunity. The Journal of experimental medicine 214, 3105–3122. [PubMed: 28847868]

Gutierrez-Martinez E, Planes R, Anselmi G, Reynolds M, Menezes S, Adiko AC, Saveanu L, and Guermonprez P. (2015). Cross-Presentation of Cell-Associated Antigens by MHC Class I in Dendritic Cell Subsets. Frontiers in immunology 6, 363. [PubMed: 26236315]

Heng TS, and Painter MW (2008). The Immunological Genome Project: networks of gene expression in immune cells. Nat Immunol 9, 1091–1094. [PubMed: 18800157]

Hodi FS, Butler M, Oble DA, Seiden MV, Haluska FG, Kruse A, Macrae S, Nelson M, Canning C, Lowy I, et al. (2008). Immunologic and clinical effects of antibody blockade of cytotoxic T lymphocyte-associated antigen 4 in previously vaccinated cancer patients. Proceedings of the National Academy of Sciences of the United States of America 105, 3005–3010. [PubMed: 18287062]

Huang AC, Postow MA, Orlowski RJ, Mick R, Bengsch B, Manne S, Xu W, Harmon S, Giles JR, Wenz B, et al. (2017). T-cell invigoration to tumour burden ratio associated with anti-PD-1 response. Nature 545, 60–65. [PubMed: 28397821]

Johnson DB, Estrada MV, Salgado R, Sanchez V, Doxie DB, Opalenik SR, Vilgelm AE, Feld E, Johnson AS, Greenplate AR, et al. (2016). Melanoma-specific MHC-II expression represents a tumour-autonomous phenotype and predicts response to anti-PD-1/PD-L1 therapy. Nature communications 7, 10582.

Josefowicz SZ, Lu LF, and Rudensky AY (2012). Regulatory T cells: mechanisms of differentiation and function. Annual review of immunology 30, 531–564.

Krappmann D, Wegener E, Sunami Y, Esen M, Thiel A, Mordmuller B, and Scheidereit C. (2004). The IkappaB kinase complex and NF-kappaB act as master regulators of lipopolysaccharide-induced gene expression and control subordinate activation of AP-1. Molecular and cellular biology 24, 6488–6500. [PubMed: 15226448]

Krishnaswamy JK, Gowthaman U, Zhang B, Mattsson J, Szeponik L, Liu D, Wu R, White T, Calabro S, Xu L, et al. (2017). Migratory CD11b(+) conventional dendritic cells induce T follicular helper cell-dependent antibody responses. Science immunology 2.

Kumamoto Y, Hirai T, Wong PW, Kaplan DH, and Iwasaki A. (2016). CD301b(+) dendritic cells suppress T follicular helper cells and antibody responses to protein antigens. eLife 5.

Kumamoto Y, Linehan M, Weinstein JS, Laidlaw BJ, Craft JE, and Iwasaki A. (2013). CD301b(+) dermal dendritic cells drive T helper 2 cell-mediated immunity. Immunity 39, 733–743. [PubMed: 24076051]

Laidlaw BJ, Craft JE, and Kaech SM (2016). The multifaceted role of CD4(+) T cells in CD8(+) T cell memory. Nat Rev Immunol 16, 102–111. [PubMed: 26781939]

Laoui D, Keirsse J, Morias Y, Van Overmeire E, Geeraerts X, Elkrim Y, Kiss M, Bolli E, Lahmar Q, Sichien D, et al. (2016). The tumour microenvironment harbours ontogenically distinct dendritic cell populations with opposing effects on tumour immunity. Nature communications 7, 13720.

Larkin J, Chiarion-Sileni V, Gonzalez R, Grob JJ, Cowey CL, Lao CD, Schadendorf D, Dummer R, Smylie M, Rutkowski P, et al. (2015). Combined Nivolumab and Ipilimumab or Monotherapy in Untreated Melanoma. The New England journal of medicine 373, 23–34. [PubMed: 26027431]

Lavin Y, Kobayashi S, Leader A, Amir ED, Elefant N, Bigenwald C, Remark R, Sweeney R, Becker CD, Levine JH, et al. (2017). Innate Immune Landscape in Early Lung Adenocarcinoma by Paired Single-Cell Analyses. Cell 169, 750–765.e717. [PubMed: 28475900]

Liang J, Huang HI, Benzatti FP, Karlsson AB, Zhang JJ, Youssef N, Ma A, Hale LP, and Hammer GE (2016). Inflammatory Th1 and Th17 in the Intestine Are Each Driven by Functionally Specialized Dendritic Cells with Distinct Requirements for MyD88. Cell reports 17, 1330–1343. [PubMed: 27783947]

Mandal R, Senbabaoglu Y, Desrichard A, Havel JJ, Dalin MG, Riaz N, Lee KW, Ganly I, Hakimi AA, Chan TA, et al. (2016). The head and neck cancer immune landscape and its immunotherapeutic implications. JCI insight 1, e89829.

Merad M, Sathe P, Helft J, Miller J, and Mortha A. (2013). The dendritic cell lineage: ontogeny and function of dendritic cells and their subsets in the steady state and the inflamed setting. Annual review of immunology 31, 563–604.

Meredith MM, Liu K, Darrasse-Jeze G, Kamphorst AO, Schreiber HA, Guermonprez P, Idoyaga J, Cheong C, Yao KH, Niec RE, et al. (2012). Expression of the zinc finger transcription factor zDC (Zbtb46, Btbd4) defines the classical dendritic cell lineage. The Journal of experimental medicine 209, 1153–1165. [PubMed: 22615130]

Miller JC, Brown BD, Shay T, Gautier EL, Jojic V, Cohain A, Pandey G, Leboeuf M, Elpek KG, Helft J, et al. (2012). Deciphering the transcriptional network of the dendritic cell lineage. Nat Immunol 13, 888–899. [PubMed: 22797772]

Nirschl CJ, Suarez-Farinas M, Izar B, Prakadan S, Dannenfelser R, Tirosh I, Liu Y, Zhu Q, Devi KSP, Carroll SL, et al. (2017). IFNγamma-Dependent Tissue-Immune Homeostasis Is Co-opted in the Tumor Microenvironment. Cell 170, 127–141.e115. [PubMed: 28666115]

Ochiai S, Roediger B, Abtin A, Shklovskaya E, Fazekas de St Groth B, Yamane H, Weninger W, Le Gros G, and Ronchese F. (2014). CD326(lo)CD103(lo)CD11b(lo) dermal dendritic cells are activated by thymic stromal lymphopoietin during contact sensitization in mice. Journal of immunology (Baltimore, Md : 1950) 193, 2504–2511.

Pandiyan P, Zheng L, Ishihara S, Reed J, and Lenardo MJ (2007). CD4+CD25+Foxp3+ regulatory T cells induce cytokine deprivation-mediated apoptosis of effector CD4+ T cells. Nat Immunol 8, 1353–1362. [PubMed: 17982458]

Pauken KE, Sammons MA, Odorizzi PM, Manne S, Godec J, Khan O, Drake AM, Chen Z, Sen DR, Kurachi M, et al. (2016). Epigenetic stability of exhausted T cells limits durability of reinvigoration by PD-1 blockade. Science (New York, NY) 354, 1160–1165.

Philip M, Fairchild L, Sun L, Horste EL, Camara S, Shakiba M, Scott AC, Viale A, Lauer P, Merghoub T, et al. (2017). Chromatin states define tumour-specific T cell dysfunction and reprogramming. Nature 545, 452–456. [PubMed: 28514453]

Puram SV, Tirosh I, Parikh AS, Patel AP, Yizhak K, Gillespie S, Rodman C, Luo CL, Mroz EA, Emerick KS, et al. (2017). Single-Cell Transcriptomic Analysis of Primary and Metastatic Tumor Ecosystems in Head and Neck Cancer. Cell 171, 1611–1624.e1624. [PubMed: 29198524]

Quezada SA, Simpson TR, Peggs KS, Merghoub T, Vider J, Fan X, Blasberg R, Yagita H, Muranski P, Antony PA, et al. (2010). Tumor-reactive CD4(+) T cells develop cytotoxic activity and eradicate large established melanoma after transfer into lymphopenic hosts. The Journal of experimental medicine 207, 637–650. [PubMed: 20156971]

Qureshi OS, Zheng Y, Nakamura K, Attridge K, Manzotti C, Schmidt EM, Baker J, Jeffery LE, Kaur S, Briggs Z, et al. (2011). Trans-endocytosis of CD80 and CD86: a molecular basis for the cell-extrinsic function of CTLA-4. Science (New York, NY) 332, 600–603.

Roberts Edward W., Broz Miranda L., Binnewies M, Headley Mark B., Nelson Amanda E., Wolf Denise M., Kaisho T, Bogunovic D, Bhardwaj N, and Krummel Matthew F. (2016). Critical Role for CD103+/CD141+ Dendritic Cells Bearing CCR7 for Tumor Antigen Trafficking and Priming of T Cell Immunity in Melanoma. Cancer Cell 30, 324–336. [PubMed: 27424807]

Ruffell B, Chang-Strachan D, Chan V, Rosenbusch A, Ho CMT, Pryer N, Daniel D, Hwang ES, Rugo HS, and Coussens LM (2014). Macrophage IL-10 blocks CD8+ T cell-dependent responses to chemotherapy by suppressing IL-12 expression in intratumoral dendritic cells. Cancer Cell 26, 623–637. [PubMed: 25446896]

Salmon H, Idoyaga J, Rahman A, Leboeuf M, Remark R, Jordan S, Casanova-Acebes M, Khudoynazarova M, Agudo J, Tung N, et al. (2016). Expansion and Activation of CD103+ Dendritic Cell Progenitors at the Tumor Site Enhances Tumor Responses to Therapeutic PD-L1 and BRAF Inhibition. Immunity 44, 924–938. [PubMed: 27096321]

Satpathy AT, Kc W, Albring JC, Edelson BT, Kretzer NM, Bhattacharya D, Murphy TL, and Murphy KM (2012). Zbtb46 expression distinguishes classical dendritic cells and their committed progenitors from other immune lineages. The Journal of experimental medicine 209, 1135–1152. [PubMed: 22615127]

Schietinger A, Philip M, Krisnawan VE, Chiu EY, Delrow JJ, Basom RS, Lauer P, Brockstedt DG, Knoblaugh SE, Hämmerling GJ, et al. (2016). Tumor-Specific T Cell Dysfunction Is a Dynamic Antigen-Driven Differentiation Program Initiated Early during Tumorigenesis. Immunity 45, 389–401. [PubMed: 27521269]

Schlitzer A, Sivakamasundari V, Chen J, Sumatoh HR, Schreuder J, Lum J, Malleret B, Zhang S, Larbi A, Zolezzi F, et al. (2015). Identification of cDC1- and cDC2-committed DC progenitors reveals early lineage priming at the common DC progenitor stage in the bone marrow. Nat Immunol 16, 718–728. [PubMed: 26054720]

Shang B, Liu Y, Jiang SJ, and Liu Y. (2015). Prognostic value of tumor-infiltrating FoxP3+ regulatory T cells in cancers: a systematic review and meta-analysis. Scientific reports 5, 15179. [PubMed: 26462617]

Shiow LR, Rosen DB, Brdickova N, Xu Y, An J, Lanier LL, Cyster JG, and Matloubian M. (2006). CD69 acts downstream of interferon-alpha/beta to inhibit S1P1 and lymphocyte egress from lymphoid organs. Nature 440, 540–544. [PubMed: 16525420]

Spranger S, Dai D, Horton B, and Gajewski TF (2017). Tumor-Residing Batf3 Dendritic Cells Are Required for Effector T Cell Trafficking and Adoptive T Cell Therapy. Cancer Cell 31, 711–723 e714. [PubMed: 28486109]

Sun S, Zhang X, Tough DF, and Sprent J. (1998). Type I interferon-mediated stimulation of T cells by CpG DNA. The Journal of experimental medicine 188, 2335–2342. [PubMed: 9858519]

Topalian SL, Sznol M, McDermott DF, Kluger HM, Carvajal RD, Sharfman WH, Brahmer JR, Lawrence DP, Atkins MB, Powderly JD, et al. (2014). Survival, durable tumor remission, and long-term safety in patients with advanced melanoma receiving nivolumab. Journal of clinical oncology : official journal of the American Society of Clinical Oncology 32, 1020–1030. [PubMed: 24590637]

Tumeh PC, Harview CL, Yearley JH, Shintaku IP, Taylor EJ, Robert L, Chmielowski B, Spasic M, Henry G, Ciobanu V, et al. (2014). PD-1 blockade induces responses by inhibiting adaptive immune resistance. Nature 515, 568–571. [PubMed: 25428505]

Tussiwand R, Everts B, Grajales-Reyes GE, Kretzer NM, Iwata A, Bagaitkar J, Wu X, Wong R, Anderson DA, Murphy TL, et al. (2015). Klf4 expression in conventional dendritic cells is required for T helper 2 cell responses. Immunity 42, 916–928. [PubMed: 25992862]

Villani AC, Satija R, Reynolds G, Sarkizova S, Shekhar K, Fletcher J, Griesbeck M, Butler A, Zheng S, Lazo S, et al. (2017). Single-cell RNA-seq reveals new types of human blood dendritic cells, monocytes, and progenitors. Science (New York, NY) 356.

Wallin JJ, Bendell JC, Funke R, Sznol M, Korski K, Jones S, Hernandez G, Mier J, He X, Hodi FS, et al. (2016). Atezolizumab in combination with bevacizumab enhances antigen-specific T-cell migration in metastatic renal cell carcinoma. Nature communications 7, 12624.

Wei SC, Levine JH, Cogdill AP, Zhao Y, Anang NAS, Andrews MC, Sharma P, Wang J, Wargo JA, Pe'er D, et al. (2017). Distinct Cellular Mechanisms Underlie Anti-CTLA-4 and Anti-PD-1 Checkpoint Blockade. Cell 170, 1120–1133.e1117. [PubMed: 28803728]

Zappasodi R, Budhu S, Hellmann MD, Postow MA, Senbabaoglu Y, Manne S, Gasmi B, Liu C, Zhong H, Li Y, et al. (2018). Non-conventional Inhibitory CD4(+)Foxp3(−)PD-1(hi) T Cells as a Biomarker of Immune Checkpoint Blockade Activity. Cancer Cell 33, 1017–1032.e1017. [PubMed: 29894689]

Zou T, Caton AJ, Koretzky GA, and Kambayashi T. (2010). Dendritic cells induce regulatory T cell proliferation through antigen-dependent and -independent interactions. Journal of immunology (Baltimore, Md : 1950) 185, 2790–2799.

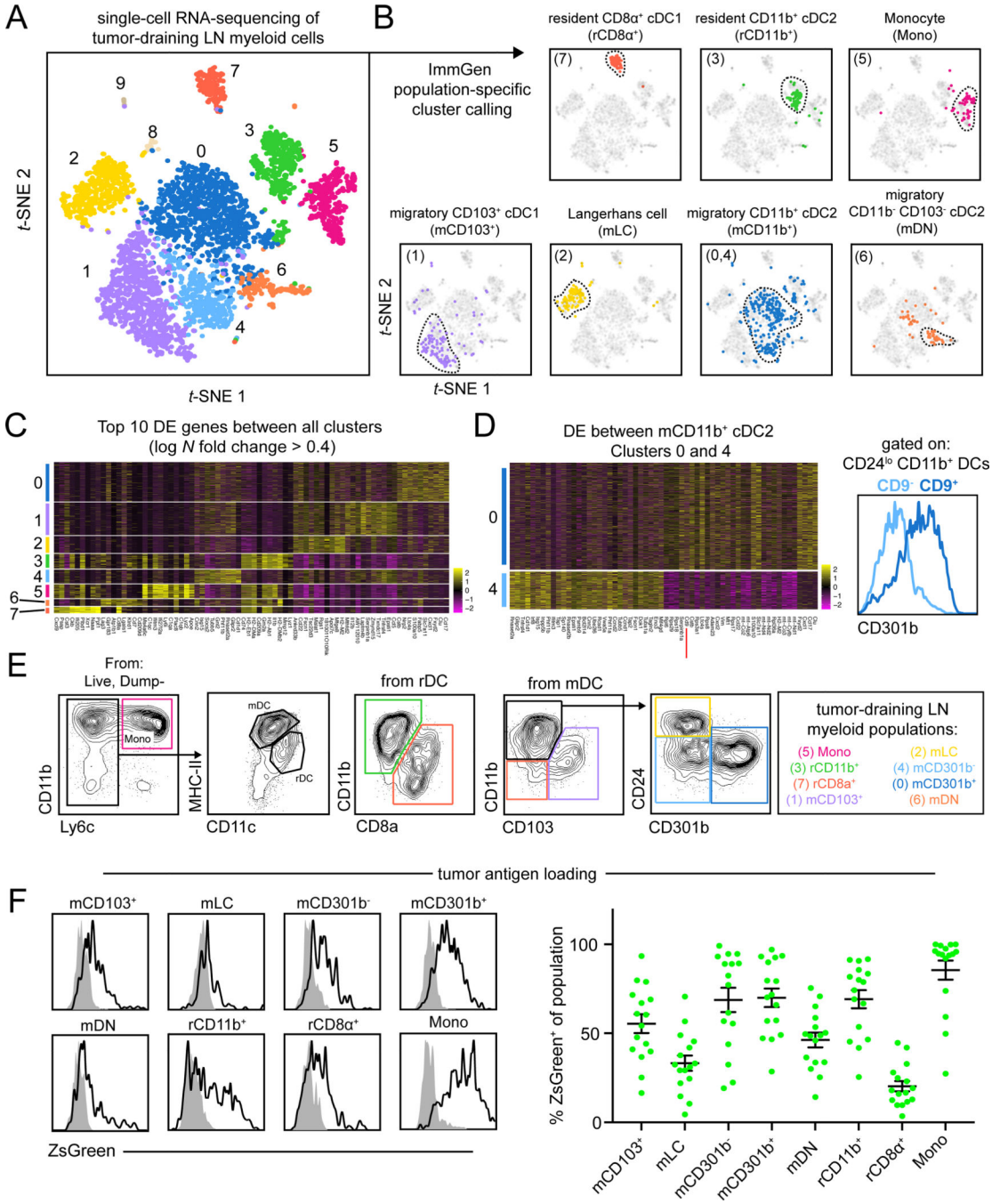

Figure 1.

Unbiased scRNA-seq of myeloid cells in the tdLN reveals extensive heterogeneity.

(A) *t*-SNE display and graph-based clustering of CD90.2^{-} B220^{-} NK1.1^{-} CD11b^{+} and/or CD11c^{+} myeloid cells sorted from B16F10 tdLN and processed for scRNA-seq. Each dot represents a single cell. **(B)** Expression of ImmGen population-specific gene signatures distributed across *t*-SNE plot of (A). **(C)** Heatmap displaying top 10 DE genes for each cluster when comparing clusters 0 through 7 (ranked by fold change) **(D) (left)** A heatmap displaying the top 30 DE genes between clusters 0 and 4, with *Cd9* highlighted by a red line.

(right) A flow cytometry histogram displaying the differential surface expression of CD301b between $CD9^{-}$ and $CD9^{+}$ $CD11b^{+}$ $CD24^{-}$ DCs **(E)** Representative gating strategy used to identify myeloid populations in the tdLN **(F)** Representative flow cytometry histograms displaying levels of ZsGreen tumor antigen within myeloid populations in the tdLN **(left)**. Frequency of $ZsGreen^{+}$ cells within t dLN myeloid populations **(right)**. Data pooled from two independent experiments. Figure 2

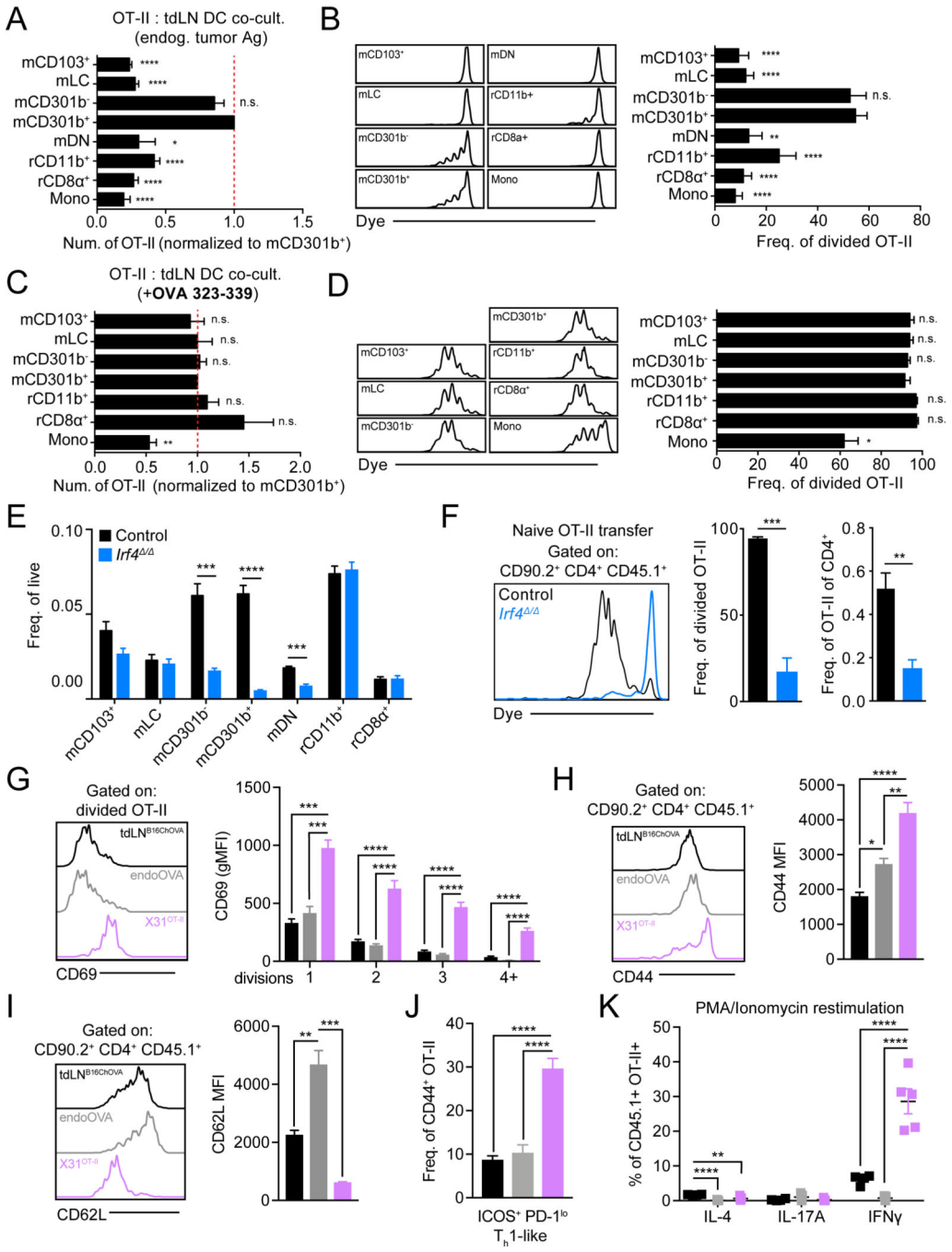

Figure 2.

mCD301b$^{-/+}$ cDC2 are uniquely able to induce anti-tumor CD4^{+} T$_{conv}$ proliferation but fail to initiate CD4^{+} T$_{conv}$ differentiation.

(**A-D**) Purified CD4^{+} OT-II T cells were co-cultured *ex vivo* with sorted APC populations from tdLN and analyzed at 3 days. **(A)** Absolute number of live OT-II T cells recovered from co-culture, normalized and statistically compared to mCD301b^{+} condition (t-test). **(B)** Histograms of OT-II T cell dye dilution **(left)**. Frequency of recovered OT-II T cells that had undergone division with statistical comparison to mCD301b^{+} condition (t-test) **(right)**. **(C)**

Absolute number of live OT-II T cells recovered from co-culture containing exogenous OVA peptide (323–339), normalized and statistically compared to mCD301b$^+$ condition (t-test). **(D)** Histograms of OT-II T cell dye dilution **(left)**. Frequency of recovered OT-II T cells that had undergone division with statistical comparison to mCD301b$^+$ condition (t-test) **(right)**. **(E)** Frequency of tdLN DC populations in control or *Irf4*$^{-/-}$ tumor-bearing mice. **(F)** Purified CD45.1$^+$ OT-II T cells were adoptively transferred to control or *Irf4*$^{-/-}$ B16^{ChOVA} tumor-bearing mice with tdLN harvested 3 days later to assess OT-II T cell dye dilution **(left)** and quantify the frequency of cells that had divided (**middle**) and their frequency of endogenous CD4$^+$ T cells **(right)**. (**G-K**) CD45.1$^+$ CD4$^+$ OT-II T cells were transferred to wild-type mice that were inoculated with B16^{chOVA} (tdLN^{B16ChOVA}), endoOVA, or X31^{pOVA} and draining LNs were harvested for analysis. **(G)** Cell surface Cd69 levels on divided CD45.1$^+$ CD4$^+$ OT-II T cells **(left)** and quantification of MFI with each cell division as determined by dye dilution **(right)** 3 days following transfer. Surface CD44 **(H)** and CD62L **(I)** levels on transferred CD45.1$^+$ CD4$^+$ OT-II T cells **(left)** and quantification of MFI **(right)** 3 days following transfer. **(J)** Frequency of transferred CD45.1$^+$ CD4$^+$ CD44$^+$ OT-II T cells that are ICOS$^+$PD-1^{lo} T_h1-like. **(K)** Frequency of transferred CD45.1$^+$ CD4$^+$ CD44$^+$ OT-II T cells that produce IL-4, IL-17A and IFNγ following PMA/Ionomycin restimulation with detection by intracellular antibody staining 7 days after transfer. Data are represented as average ± SEM unless explicitly specified. *P <0.05, **P<0.01, ***P<0.001, ****P<0.0001.

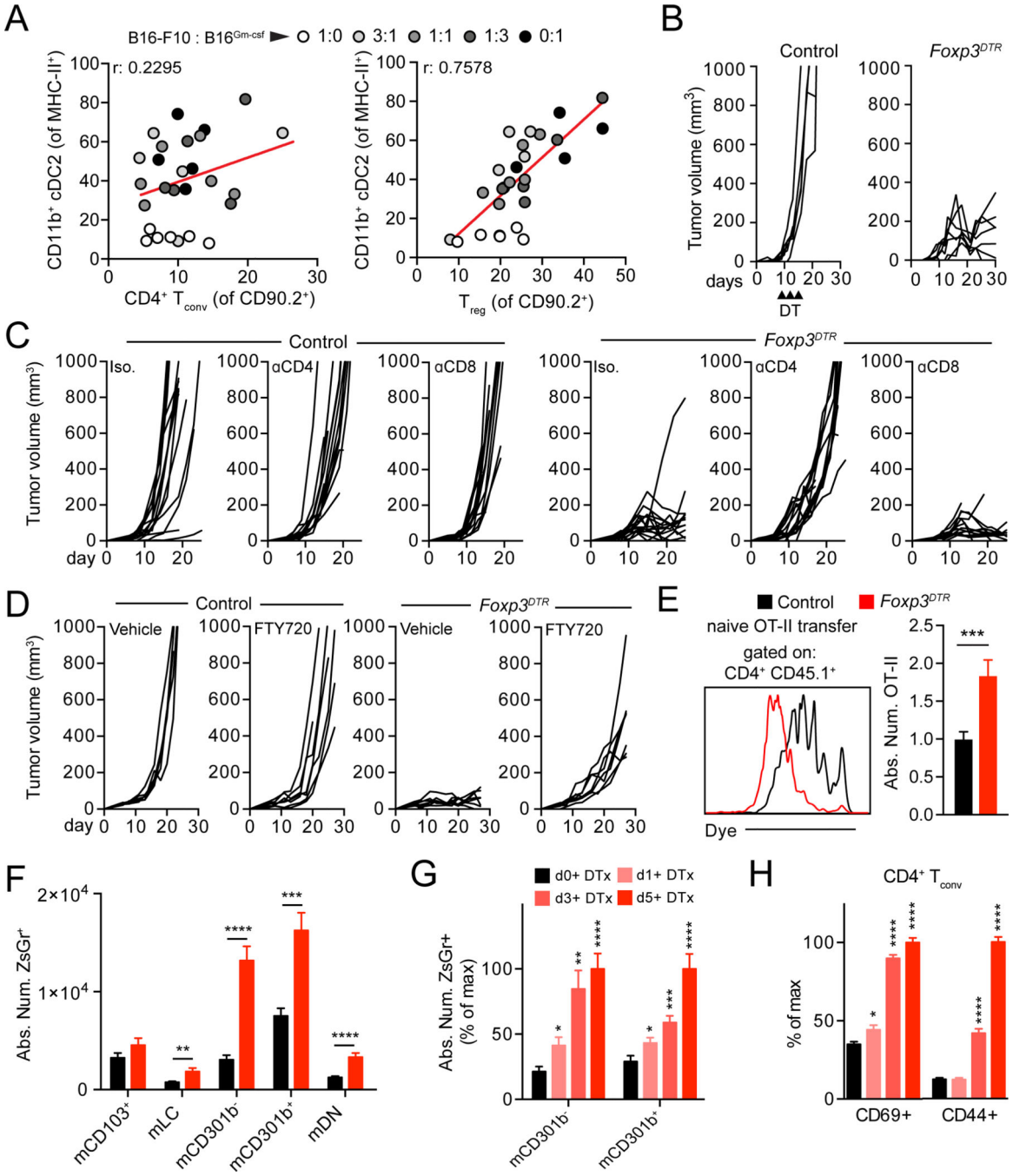

Figure 3.

Regulatory T cell depletion enhances cDC2 migration to the tdLN and unleashes an anti-tumor $CD4^+$ T_{conv} response. **(A)** Dot plot correlation of intratumoral $CD11b^+$ $CD301b^{-/+}$ cDC2 frequency within $MHC\text{-}II^+$ cells against $CD4^+$ T_{conv} within $CD90.2^+$ **(left)** or T_{reg} **(right)** within $CD90.2^+$. Dots colored according to ratio of B16-F10:$B16^{Gm\text{-}csf}$ cells in the tumor. Two pooled experiments displayed. **(B)** Tumor growth from control and *Foxp3*^{DTR} mice. Upward facing black arrowheads indicate DT treatment. Results depict tumor growth curves of individual mice. **(C)** Tumor growth from control or *Foxp3*^{DTR} mice injected with

isotype/anti-CD4/anti-CD8 depleting antibodies. Results depict tumor growth curves of individual mice. Two pooled experiments displayed. **(D)** Tumor growth from control or *Foxp3*^{DTR} mice injected with with vehicle or FTY720. Results depict tumor growth curves of individual mice. Two pooled experiment displayed. **(E)** CD45.1^{+} CD4^{+} OT-II T cells were adoptively transferred into DT-treated control or *Foxp3*^{DTR} B16^{ChOVA}-tumor-bearing mice and recovered 3 days later for analysis of dye dilution **(left)** and quantification of absolute number of OT-II present within the tdLN **(right)**. Three pooled experiments displayed with normalization to control. **(F)** Control and *Foxp3*^{DTR} B16^{ZsGreen} tumor-bearing mice were treated with DT and absolute number of ZsGreen^{+} migratory DC in the tdLN were analyzed at day 5 post-DT. **(G)** Control and *Foxp3*^{DTR} B16^{ZsGreen} tumor-bearing mice were treated with DT and absolute number of ZsGreen^{+} CD11b^{+} cDC2 in the tdLN were analyzed at day 0, 1, 3 and 5 post-DT. Data displayed as percent of maximum absolute number. Samples statistically compared to day 0 DT condition. **(H)** Control and *Foxp3*^{DTR} B16^{ZsGreen} tumor-bearing mice were treated with DT and analyzed for the frequency of CD4^{+} T_{conv} expressing CD69 and CD44 at day 0, 1, 3 and 5 post-DT. Data displayed as frequency of maximum expression. Samples statistically compared to day 0 DT condition. Data are represented as average ± SEM. *P <0.05, **P<0.01, ***P<0.001, ****P<0.0001.

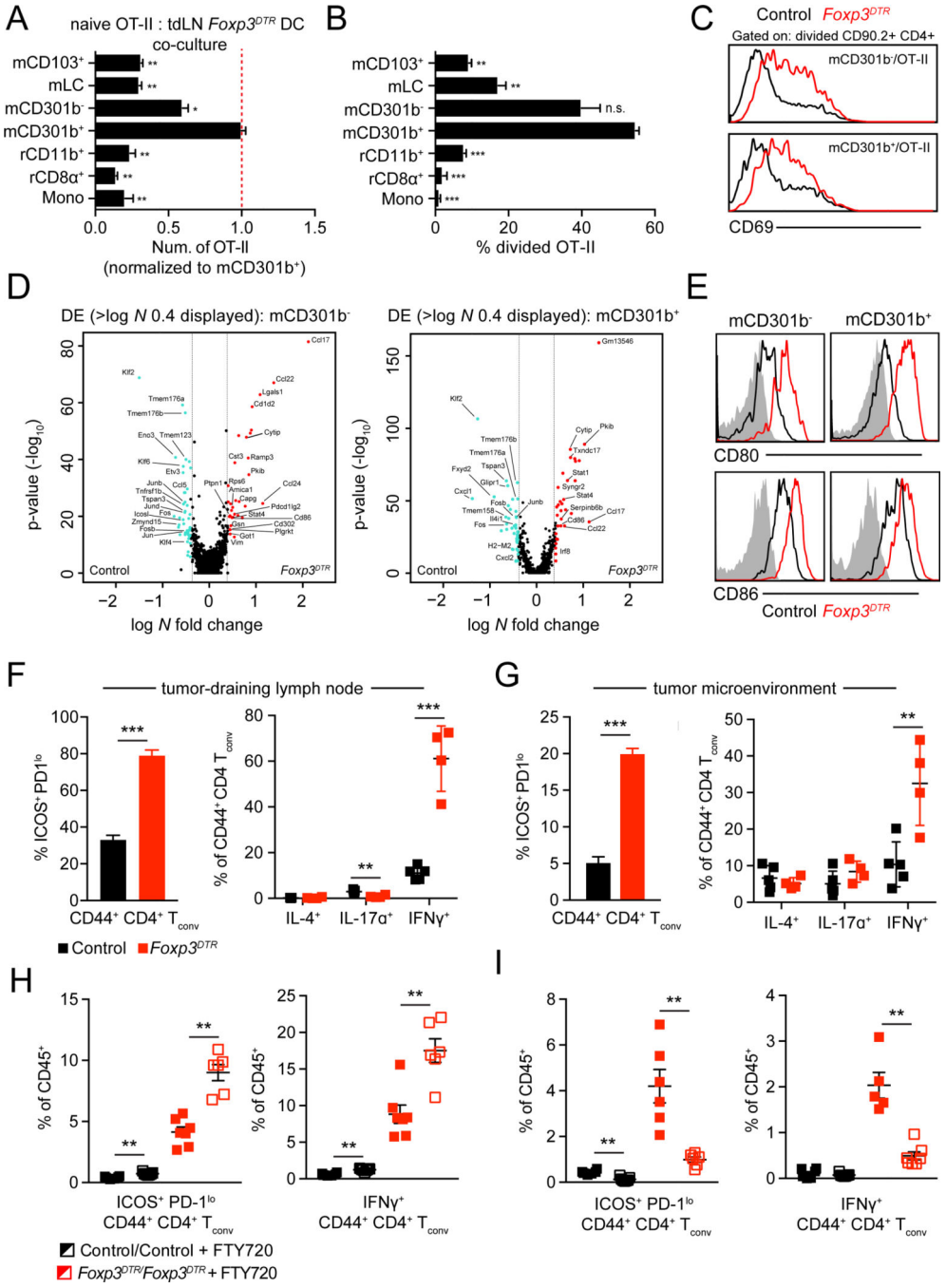

Figure 4.

Regulatory T cell depletion enhances cDC2 function and CD4$^+$ T_{conv} differentiation. (**A-C**) Purified CD4$^+$ OT-II T cells were co-cultured with tdLN APC populations sorted from tdLN of control or *Foxp3^{DTR}* B78chOVA-bearing animals and harvested 3 days after plating for analysis. **(A)** Absolute number of live OT-II T cells recovered, normalized and statistically compared to mCD301b$^+$ condition. **(B)** Frequency of recovered OT-II T cells that had undergone division, statistically compared to mCD301b$^+$ condition (t-test). **(C)** Cell surface CD69 levels on divided OT-II. **(D)** Volcano plots displaying DE expressed genes comparing

control and Foxp3DTR tdLN mCD301b^{-} **(left)** and mCD301b^{+} **(right)**. Log *N* fold cutoff of 0.4 used. Genes of interest labelled. **(E)** Cell surface levels of CD80 and CD86 on mCD301b^{-} and mCD301b^{+} in control and *Foxp3^{DTR}* tdLN. **(F)** Frequency of CD44^{+} CD4^{+} T_{conv} that are ICOS^{+} PD-1^{lo} in control and *Foxp3^{DTR}* tdLN **(left)**. Frequency of tdLN CD44^{+} CD4^{+} T_{conv} producing IL-4, IL-17A or IFNγ from control or *Foxp3^{DTR}* tumor-bearing mice following *ex vivo* restimulation **(right)**. **(G)** Frequency of CD44^{+} CD4^{+} T_{conv} that are ICOS^{+} PD-1^{lo} in control and *Foxp3^{DTR}* TME **(left)**. Frequency of CD44^{+} CD4^{+} T_{conv} producing IL-4, IL-17A or IFNγ in control or *Foxp3^{DTR}* TME following *ex vivo* restimulation **(right)**. **(H, I)** Control and *Foxp3^{DTR}* tumor-bearing mice were treated with FTY720 or vehicle and tdLN (H) or tumor (I) were harvested to quantify frequency of CD45^{+} cells that are CD44^{+} CD4^{+} ICOS^{+} PD-1^{lo} T_{conv} **(left)** and are IFNγ-producing CD44^{+} CD4^{+} T_{conv} following *ex vivo* restimulation **(right)**. Representative experiment displayed. Data are represented as average ± SEM. *P <0.05, **P<0.01, ***P<0.001, ****P<0.0001.

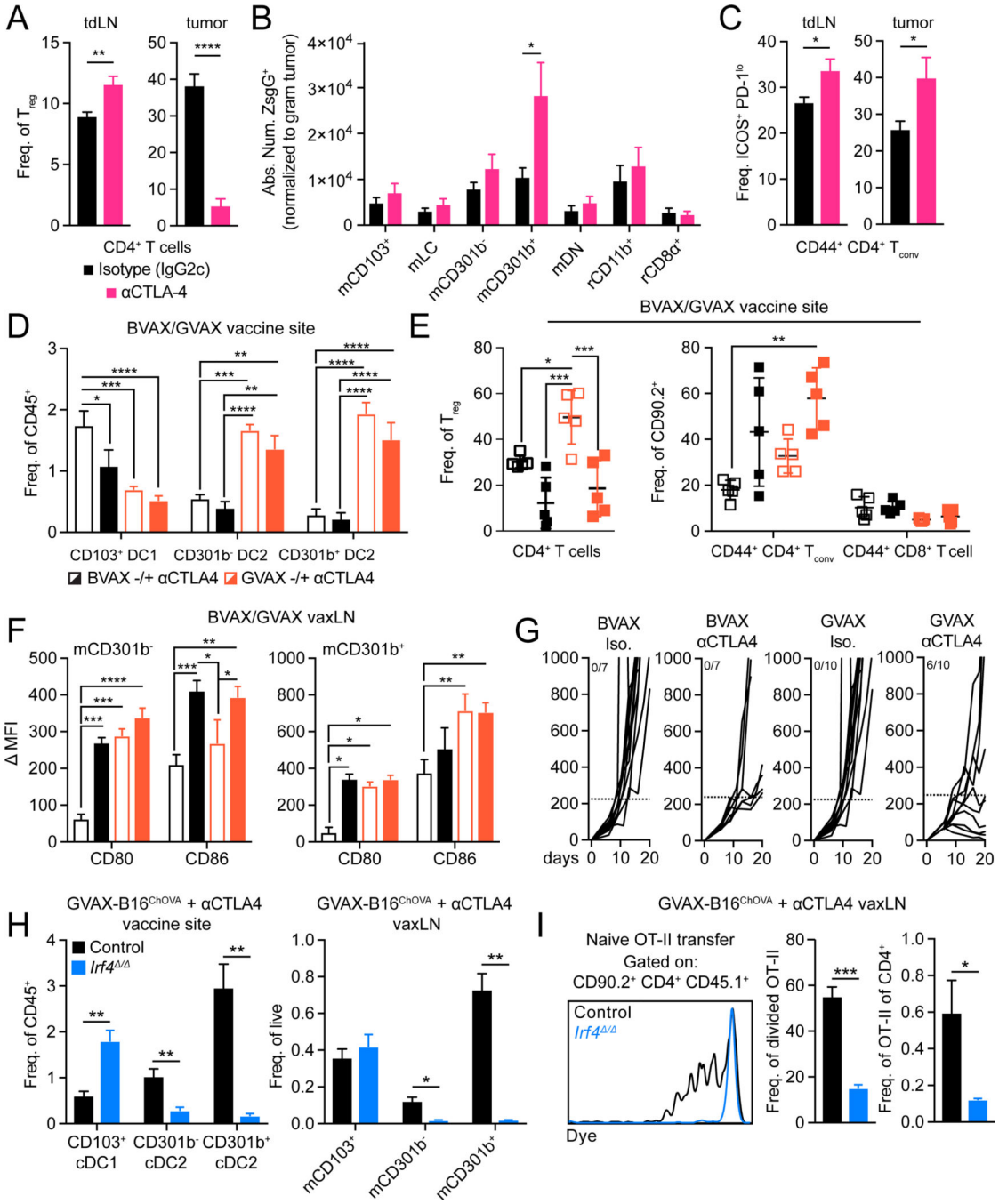

Figure 5.

Anti-CTLA-4 induces expansion and functional enhancement of CD11b^{+} cDC2. (**A**) Frequency of T_{reg} within CD4^{+} T cells in tdLN **(left)** or tumor **(right)** from B16^{ZsGreen} tumor-bearing mice treated with mouse IgG2c isotype or anti-CTLA-4 with a mouse IgG2c Fc. (**B**) Absolute number of ZsGreen^{+} DC in tdLN (normalized to weight of associated tumor). (**C**) Frequency of CD44^{+} CD4^{+} T_{conv} with ICOS^{+} PD-1^{lo} surface phenotype in tdLN (left) or tumor (right). (**D**) DC frequency of CD45^{+} cells within the vaccine site of mice treated with BvAX$^{+/-}$ αCTLA-4 or GVAX +/− αCTLA-4. (**E**) Frequency of T_{reg} amongst

CD4$^+$ T cells **(left)** and frequency of CD44$^+$ CD4$^+$ T_{conv} or CD44$^+$ cD8$^+$ T cells amongst CD90.2$^+$ T cells within the vaccine site of mice treated with BVAX +/− αCTLA-4 or GVAX +/− αCTLA-4 **(right)**. (**F**) Quantification of CD80 and CD86 DMFI on mCD301b$^-$ **(left)** or mCD301b$^+$ **(right)** within the vaxLN of mice treated with BVAX +/− αCTLA-4 or GVAX +/− αCTLA-4. (**G**) Tumor growth from mice treated with BVAX +/− αCTLA-4 or GVAX +/− αCTLA-4. Ratio represents number of mice with tumors that displayed profound response (< 250mm^3). Dotted line signifies 250 mm^3. Representative experiment displayed. (**H**) DC frequency of either CD45$^+$ or live cells within the vaccine site **(left)** or vaxLN **(right)** of control or *Irf4*$^{\Delta/\Delta}$ mice treated with GVAX-B16^{ChOVA} and anti-CTLA-4. (**I**) Purified CD45.1$^+$ OT-II T cells were adoptively transferred to control or *Irf4*$^{\Delta/\Delta}$ mice treated with GVAX-B16^{ChOVA} and anti-CTLA-4 and vavLN were harvested 3 days later to assess OT-II T cell dye dilution **(left)** and quantify the frequency of cells that had divided (**middle**) and their frequency of endogenous CD4$^+$ T cells **(right)**. Data are represented as ± average SEM. *P <0.05, **P<0.01, ***P<0.001, ****P<0.0001.

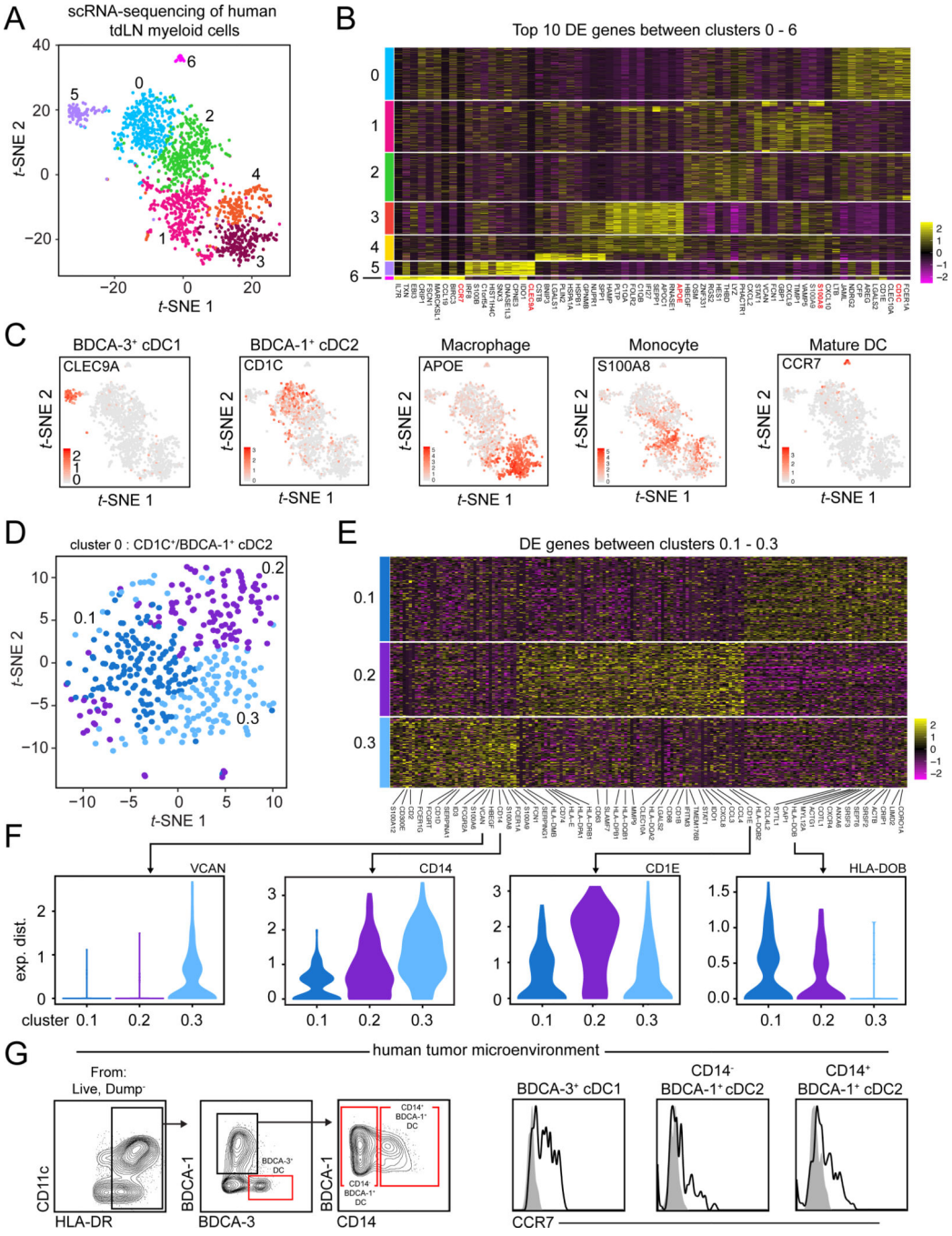

Figure 6.

scRNA-seq of the human tdLN reveals heterogeneity within BDCA-1$^+$ cDC2. **(A)** *t*-SNE display of CD45$^+$ CD3$^-$ CD19/20$^-$ CD56$^-$ myeloid cells sorted from a human melanoma tdLN and processed for scRNA-seq with pDC, neutrophil, NK cell, T cell and B cell contaminants removed from graph-based clustering analysis. (**B)** Heatmap displaying top 10 DE genes for each cluster when comparing clusters 0 through 6 (ranked by fold change). **(C)** Gene overlays of markers associated with various myeloid cell types on human tdLN *t*-SNE. **(D)** *t*-SNE display and graph-based clustering of BDCA-1$^+$ cDC2 (cluster 0) from (A). **(E)**

Heatmap displaying DE genes between clusters 0.1–0.3 with genes of interested labelled. **(F)** Violin plots displaying expression probability differences for denoted genes within clusters 0.1–0.3. **(G)** Gating strategy (**left**) in human TME to identify BDCA-3^{+} cDC1, CD14^{-} BDCA-1^{+} cDC2, CD14^{+} BDCA-1^{+} cDC2. Cell surface expression of CCR7 on BDCA-3^{+} cDC1, CD14^{-} BDCA-1^{+} cDC2, CD14^{+} BDCA-1^{+} cDC2 (**right**).

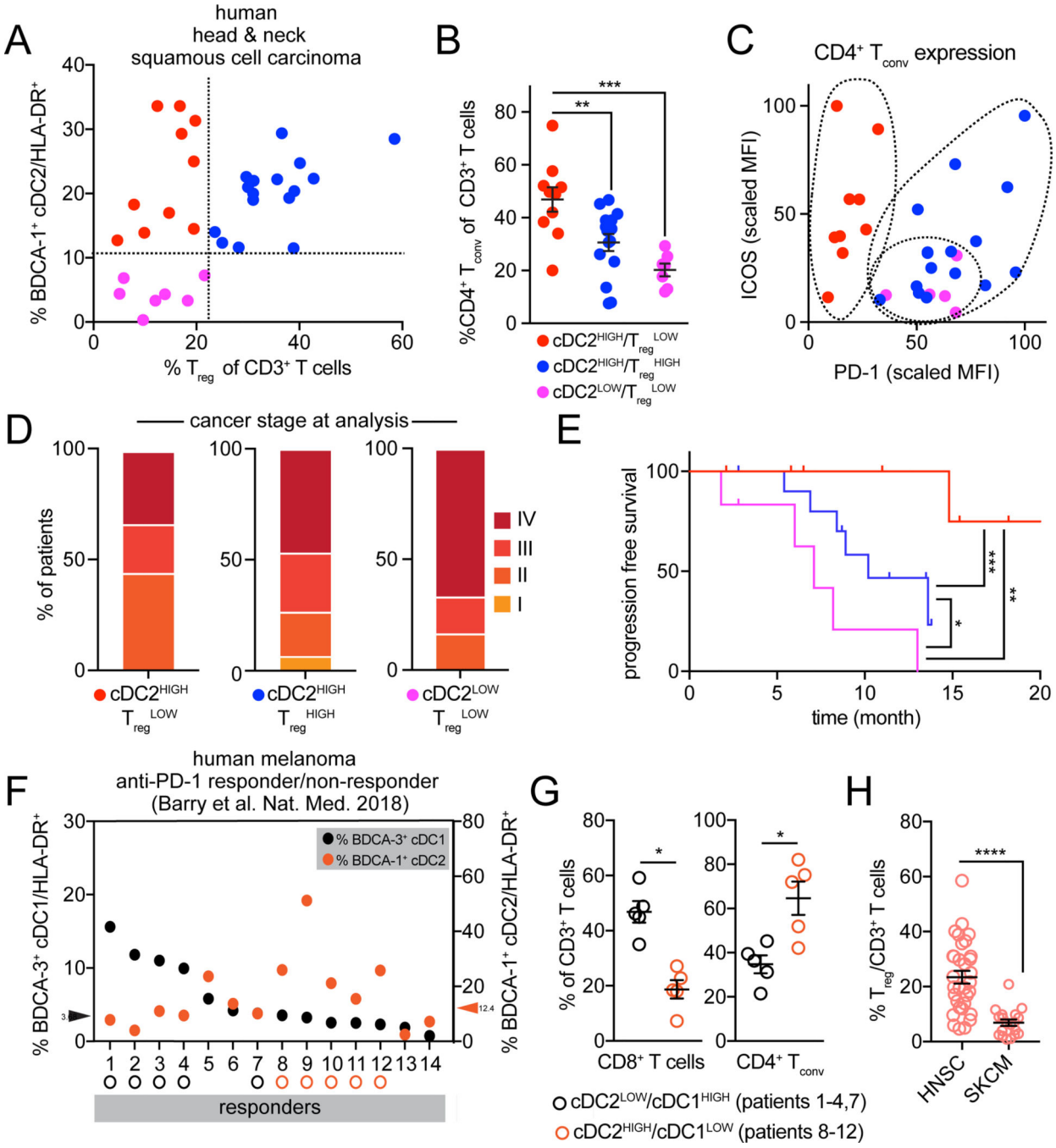

Figure 7.

BDCA-1$^+$ cDC2 proportion in the human TME impacts CD4$^+$ T_{conv} proportion and quality. (**A**) Dot plot of BDCA-1$^+$ cDC2 frequency of HLA-DR$^+$ cells and T_{reg} frequency of CD3$^+$ T cells as quantified by flow cytometry in 32 human HNSC tumor samples. Dotted lines represent demarcation of samples divided based on proportion of BDCA-1$^+$ cDC2 (CD14$^{-/+}$) and T_{reg}. (**B**) The frequency of CD4$^+$ T cells (of CD3$^+$ T cells) within each type of TME identified in (A). (**C**) Surface expression of ICOS and PD-1 on CD4$^+$ T_{conv}, as a normalized geometric MFI, within each type of human TME identified in (A). (**D**) Percent

of patients with a given stage of cancer at the time of flow cytometric analysis. (**E**) Progression-free survival since disease diagnosis. Mantel-Cox test performed between groups. (**F**) 19 human melanoma tumor samples (14 anti-PD-1 responder, 5 anti-PD-1 non-responders – see S6E) were parsed based on abundance of BDCA-3^+ cDC1 and plotted for proportions of both BDCA-3^+ cDC1 (black) and BDCA-1^+ cDC2 (orange). Responders were parsed based on those high for either BDCA-3^+ cDC1 (above median split of 3.63) or BDCA-1^+ cDC2 (above median split of 12.4). (**G**) Frequency of $CD3^+$ T cells that are $CD8^+$ T cells **(left)** and $CD4^+$ T_{conv} **(right)** from the two groups identified in (F). (**H**) Proportions of T_{reg} amongst $CD3^+$ T cells in samples from HNSC (A-E) and skin cutaneous melanoma (SKCM) (includes anti-PD-1 responders and non-responders) (F, G). Data are represented as ± average SEM. *P <0.05, **P<0.01, ***P<0.001, ****P<0.0001.

KEY RESOURCES TABLE

REAGENT or RESOURCE	SOURCE	IDENTIFIER
Antibodies		
anti-mouse CD11c BV650 (clone N418)	Biolegend	117339
anti-mouse/human CD11b BV605 (clone M1/70)	Biolegend	101257
anti-mouse CD103 BV421 (clone 2E7)	Biolegend	121421
anti-mouse Ly-6C BV711 (clone HK1.4)	Biolegend	128037
anti-mouse CD90.2 BV785 (clone 30-H12)	Biolegend	105331
anti-mouse/human CD45R/B220 BV785 (clone RA3-6B2)	Biolegend	103246
anti-mouse Ly-6G BV785 (clone IA8)	Biolegend	127645
anti-mouse Siglec F BV786 (clone E50-2440)	BD Biosciences	740956
anti-mouse NK1.1 BV785 (clone PK136)	Biolegend	108749
anti-mouse CD24 PE/Cy7 (clone M1/69)	Biolegend	101822
anti-mouse MHC-II AF700 (clone M5/114.15.2)	Biolegend	107622
anti-mouse CD301b PE or APC (clone URA-1)	Biolegend	146814, 146803
anti-mouse CD8a PerCP/Cy5.5 or PE/Cy7 (clone 53-6.7)	Biolegend	100734, 100722
anti-mouse F4/80 FITC (clone BM8)	Biolegend	123107
anti-mouse CD45 PerCP/Cy5.5 (clone A20)	Biolegend	110727
anti-mouse CD197/CCR7 PE	Biolegend	120105
anti-mouse CD9 AF647 (clone MZ3)	Biolegend	124809
anti-mouse CD135/FLT3 PE (clone A2F10)	Biolegend	135305
anti-mouse CD172a/SIRPA PE or AF488 (clone P84)	Biolegend	144011,144023
anti-mouse CD14 PE (clone Sa14-2)	Biolegend	123309
anti-mouse CD16/32 PE (clone 93)	Biolegend	101307
anti-mouse CD200R PE (clone OX110)	Biolegend	123907
anti-mouse CD206 PE (clone C068C2)	Biolegend	141705
anti-mouse B7-H1 PE (PD-L1/CD274) (clone 10F.9G2)	Biolegend	124307
anti-mouse B7-H2 PE (ICOS-L/CD275) (clone HK5.3)	Biolegend	107405
anti-mouse B7-H3 PE (CD276) (clone RTAA15)	Biolegend	123507
anti-mouse B7-DC (PD-L2/CD273) PE (clone TY25)	Biolegend	107205
anti-mouse CD85K (LILRB4) PE	Biolegend	144903
anti-mouse CD4 BUV395 (clone GK1.5)	BD Biosciences	563790
anti-mouse/rat/human CD278/ICOS APC (clone C398.4A)	Biolegend	313510
anti-mouse CD279/PD-1 PE (clone RMP1-14)	Biolegend	114118
anti-mouse/human CD44 BV711 (clone IM7)	Biolegend	103057
anti-mouse CD69 BV650 (clone H1.2F3)	Biolegend	104541
anti-mouse Foxp3 eF450 (clone FJK-16s)	Thermo Fisher	48-5773-82
anti-mouse/rat/human Foxp3 AF647 (clone 150D)	Biolegend	320014
anti-mouse IL-4 PE (clone 11B11)	Biolegend	504104

REAGENT or RESOURCE	SOURCE	IDENTIFIER
anti-mouse IL-17a BV421 (clone TC11-18H10.1)	Biolegend	506926
anti-mouse IFNg PE/Cy7 (clone XMG1.2)	Biolegend	505825
anti-mouse/human T-bet BV605 (clone 4B10)	Biolegend	644817
anti-mouse CD117 APC (clone 2B8)	Biolegend	105811
anti-mouse CD115 PerCP/Cy5.5 (clone AFS98)	Biolegend	135525
anti-mouse Ly6-G (clone IA8)	Biolegend	127603
anti-mouse CD3e (clone 145-2C11)	Biolegend	100303
anti-mouse CD127 (clone A7R34)	Biolegend	135005
anti-mouse NK1.1 (clone PK136)	Biolegend	108703
anti-mouse/human CD45R (RA3-6B2)	Biolegend	103203
anti-mouse TER-119 (clone TER-119)	Biolegend	116203
anti-mouse TCR γ/δ (clone GL3)	Biolegend	118103
Streptavidin BV421	Biolegend	405226
anti-human CD45 APC/e780 (clone HI30)	Thermo Fisher	47-0459-42
anti-human CD3e PerCP/e710 (clone OKT3)	Thermo Fisher	46-0037-42
anti-human HLA-DR BUV395 (clone G46-6)	BD Biosciences	564040
anti-human CD56 BUV737 (clone NCAM16.2)	BD Biosciences	564448
anti-human CD4 PE/Dazzle 594 (clone S3.5)	Biolegend	100455
anti-human CD8a BV605 (clone RPA-T8)	Biolegend	301039
anti-human CD127 BV650 (clone HIL-7R-M21)	BD Biosciences	563225
anti-human CD38 AF700 (clone HIT2)	Biolegend	303523
anti-human CD25 APC (clone 2A3)	BD Biosciences	340939
anti-human CD45RO PE (clone UCHL1)	BD Biosciences	561889
anti-human PD-1 BV786 (clone EH12)	BD Biosciences	563789
anti-human ICOS BV711 (clone DX29)	BD Biosciences	563833
anti-human FoxP3 PE/Cy7 (clone 236A/E7)	Thermo Fisher	25-4777-41
anti-human CTLA-4 BV421 (clone BNI3)	BD Biosciences	565931
anti-human/mouse/rat Ki67 AF488 (clone SolA15)	Thermo Fisher	11-5698-82
anti-human CD19 PerCP/e710 (clone H1B19)	Thermo Fisher	45-0199-42
anti-human CD20 PerCP/e710 (clone 2H7)	Thermo Fisher	45-0209-42
anti-human CD56 PerCP/e710 (clone CMSSB)	Thermo Fisher	46-0567-42
anti-human CD64 BUV737 (clone 10.1)	BD Biosciences	564425
anti-human CD11c AF700 (clone 3.9)	Thermo Fisher	56-0116-42
anti-human CD16 BV605 (clone 3G8)	Biolegend	302039
anti-human CD273/PDL2 BV650 (clone MIH18)	BD Biosciences	563844
anti-human/mouse TREM2 APC (clone 237920)	R&D Systems	FAB17291A
anti-human CD304 PE (clone 12C2)	Biolegend	354503
anti-human CD1C/BDCA-1 PE/Cy7 (clone L161)	Biolegend	331515
anti-human CD197 BV421 (clone G043H7)	Biolegend	353207

REAGENT or RESOURCE	SOURCE	IDENTIFIER
anti-human BDCA-3 FITC (clone AD5-14H12)	Miltenyi	130-098-843
anti-human PDL1 BV786 (clone MIH1)	BD Biosciences	563739
anti-human CD14 BV711 (clone M5E2)	Biolegend	301837
PE Rat IgG2a, k Isotype Ctrl Antibody (clone RTK2758)	Biolegend	400508
PE Rat IgG1, k Isotype Ctrl Antibody (clone RTK2071)	Biolegend	400408
APC Armenian Hamster IgG Isotype Ctrl Antibody (clone HTK888)	Biolegend	400912
BV605 Mouse IgG1, k Isotype Ctrl Antibody (clone MOPC-21)	Biolegend	400162
BV421 Mouse IgG2a, k Isotype Ctrl Antibody (clone MOPC-173)	Biolegend	400259
anti-mouse CD4 InVivoMab (clone GK1.5)	BioXCell	BE0003-1
anti-mouse CD8 InVivoMab (clone 2.43)	BioXCell	BE0061
anti-mouse CTLA-4 (CD152) InVivoMab (clone 9H10)	BioXCell	BE0131
Rat IgG2b, k InVivoMab	BioXCell	BE0090
Polyclonal Syrian hamster IgG InVivoMab	BioXCell	BE0087
anti-mouse CD16/32 InVivoMab	BioXCell	BE0307
anti-mouse CTLA-4 mouse IgG2c (modified clone 9D9)	Bristol-Myers-Squibb	
anti-mouse CTLA-4 mouse IgG1 (modified clone 9D9)	Bristol-Myers-Squibb	
mouse IgG2c isotype	Bristol-Myers-Squibb	
mouse IgG1 isotype	Bristol-Myers-Squibb	
Normal Rat Serum	Thermo Fisher	10710C
Armenian Hamster Serum	Innovative Research	IGHMA-SER
Biological Samples		
Human tumor samples	UC San Francisco	IRB # 13-12246 and 14-15342
Mouse tissue samples (LN, tumor)	UC San Francisco	IACUC: AN170208
Chemicals, Peptides, and Recombinant Proteins		
Matrigel GFR, Phenol-red free	Corning	356231
Collagenase, Type I	Worthington Biochemical	LS004197
Collagenase, Type IV	Worthington Biochemical	LS004189
DNAse I	Roche	10104159001
Liberase TL	Roche	5401020001
Human TruStain FcX	Biolegend	422302
Zombie Aqua Fixable Viability Kit	Biolegend	423102
Zombie NIR Fixable Viability Kit	Biolegend	423106
Brilliant Stain Buffer Plus	BD Biosciences	566385
Brefeldin A (BFA)	Sigma-Aldrich	B7651
Phorbol 12-myristate 13-acetate (PMA)	Sigma-Aldrich	P8139
Ionomycin	Invitrogen	I24222

REAGENT or RESOURCE	SOURCE	IDENTIFIER
Monensin Solution (1000X)	Thermo Fisher	00-4505-51
Diphtheria Toxin (unnicked)	List Biological Laboratories	150
FTY720	Cayman Chemical Company	10006292
eBioscience™ Cell Proliferation Dye eFluor™ 670		65-0840-85
Ovalbumin Endofit	Invivogen	Vac-pova
OVA peptide (323-339)	Genscript	RP10610-1
Critical Commercial Assays		
Chromium Single Cell 3' Library & Gel Bead Kit V2	10X Genomics	120237
BD Cytofix	BD Biosciences	554655
Foxp3/Transcription factor staining buffer set	Thermo Fisher	00-5523-00
EasySep Mouse $CD4^+$ T Cell Isolation kit	STEMCELL Technologies	19852
Deposited Data		
GEO XXXXXX		
Experimental Models: Cell Lines		
B16-F10	ATCC	CRL-6475
B16-ChOVA	UC San Francisco	N/A
B78-ChOVA	UC San Francisco	N/A
B16-GM-CSF	UC San Francisco	N/A
B16-ZsGreen	UC San Francisco	N/A
Experimental Models: Organisms/Strains		
Mouse: C57BL/6J	The Jackson Laboratory	000664
Mouse: B6 CD45.1 (B6.SJL-Ptprca Pepcb/BoyJ)	The Jackson Laboratory	002014
Mouse: OT-II (B6.Cg-Tg(TcraTcrb)425Cbn/J	The Jackson Laboratory	004194
Mouse: *Irf4 fl/fl (*B6.129S1-*Irf4tm1Rdf*/J)	The Jackson Laboratory	009380
Mouse: *ActB-Cre* (FVB/N-*Tmem163Tg(ACTB-cre)2Mrt*/J) received backcrossed to C57/Bl6	The Jackson Laboratory	003376
Mouse: *CD11c-Cre* (B6.Cg-Tg(Itgax-cre)1-1Reiz/J)	The Jackson Laboratory	008068
Mouse: *Cx3cr1iDTR* (B6N.129P2-*Cx3cr1tm3(DTR)Litt*/J)	The Jackson Laboratory	025629
Mouse: *Ccr7−/−* (B6.129P2(C)-*Ccr7tm1Rfor*/J)	The Jackson Laboratory	006621
Mouse: *Zbtb46GFP (*B6.129S6(C)-*Zbtb46tm1.1Kmm*/J)	The Jackson Laboratory	027618

REAGENT or RESOURCE	SOURCE	IDENTIFIER
Mouse: *Foxp3DTR (*B6.129(Cg)-*Foxp3tm3(DTR/GFP)Ayr*/J)	The Jackson Laboratory	016958
Mouse: *Xcr1DTR (*Xcr1tm2(HBEGF/Venus)Ksho)	Tsuneyasu Kaisho, Osaka University	MGI: 5544058
Mouse: *Foxp3Cre/YFP* (B6.129(Cg)-*Foxp3tm4(YFP/icre)Ayr*/J)	The Jackson Laboratory	016959
Mouse: *Itgb8fl/fl* (Itgb8tm2Lfr)	Michael Rosenblum, UC San Francisco	MGI: 3608910
Mouse: *Il-10fl/fl* (Il-10 flox)	Susan Kaech, Salk Institute. Generated by Werner Müller.	PMID: 15534372
Mouse: *Areg−/− (*Aregtm1Dle)	Marco Conti, UC San Francisco. Generated by David C. Lee.	MGI: 2176531
Software and Algorithms		
CellRanger 2.0	10X Genomics	10xgenomics.com
STAR	Dobin et.al. 2013	code.google.com/p/rna-star/.
Seurat	Satija et al. 2015	satijalab.org/seurat/
R: The Project for Statistical Computing		r-project.org